Solid-liquid Flow in Stirred Tanks: Euler-Euler / RANS Modeling

Shi, P.; Rzehak, R.;

Originally published:

June 2020

Chemical Engineering Science 227(2020), 115875

DOI: https://doi.org/10.1016/j.ces.2020.115875

Perma-Link to Publication Repository of HZDR:

https://www.hzdr.de/publications/Publ-30925

Solid-liquid Flow in Stirred Tanks: Euler-Euler / RANS Modeling

Pengyu Shi[1,2*], Roland Rzehak[1]

[1] Helmholtz-Zentrum Dresden – Rossendorf, Institute of Fluid Dynamics, Bautzner Landstrasse 400, D-01328 Dresden, Germany

[2] Technische Universität Dresden, Faculty of Mechanical Engineering, Institute of Power Engineering, D-01062 Dresden, Germany

Abstract

Stirred tanks are widely used equipment in process engineering. CFD simulations of such equipment on industrial scales are feasible within the Euler-Euler / RANS approach. In this approach, phenomena on particle scale are not resolved and, accordingly, suitable closure models are required. The present work applies a set of closure relations that originates from a comprehensive review of existing results. Focus is on the modeling of interfacial forces which include drag, lift, turbulent dispersion, and virtual mass. Specifically, new models for the drag and lift forces are considered based on the best currently available description. To validate the model a comprehensive set of experimental data including solid velocity and volume fraction as well as liquid velocity and turbulence has been assembled. The currently proposed model compares reasonably well with this dataset and shows generally better prediction compared with other model variants that originate from different combinations of force correlations.

Keywords: stirred tanks, solid-liquid flow, Euler-Euler two-fluid model, closure relations, Reynolds-stress turbulence model

[*] Corresponding author email: p.shi@hzdr.de

1 INTRODUCTION

For the purpose of suspending solid particles in a liquid, mechanically stirred tanks are commonly used in many branches of industry like chemical engineering (Sardeshpande and Ranade, 2012), biotechnology (Trad et al., 2015), and minerals processing (Wu et al., 2011). Typical applications are heterogeneously catalyzed reactions, production of bio-hydrogen, and separation by flotation. In these applications solid particles are suspended in the turbulent flow induced by an impeller, thereby enhancing the solid-liquid heat and mass transfer. The quality of suspension is the result of an intricate interplay between the two phases and the research on this topic has a long and rich history. Next to theoretical and experimental approaches, computational fluid dynamics (CFD) simulation is recently becoming a more and more important means of investigating the hydrodynamics of the solid-liquid flows in all of the mentioned fields of application (Joshi and Nandakumar 2015, Werner et al. 2014, Wang et al. 2018).

CFD simulations of solid-liquid flow on the scale of technical equipment are feasible within the Euler-Euler framework of interpenetrating continua combined with the Reynolds-averaged Navier-Stokes (RANS) turbulence models. Since phenomena occurring on the scales of individual particles or groups thereof as well as turbulence are not resolved in this approach, accurate numerical predictions rely on suitable closure relations describing the physics on the un-resolved scales. A large number of works exist, in each of which largely a different and often incomplete set of closure relations is compared to a different set of experimental data. For the limited range of conditions to which each model variant is applied, reasonable agreement with the data is mostly obtained, but due to a lack of comparability between the individual works no complete, reliable, and robust formulation has emerged so far. Moreover, usually a number of empirical parameters are involved and have been adjusted to match the particular data, which deteriorates the applicability.

To make a first step towards such a predictive model, we consider adiabatic particulate flows where only momentum is exchanged between the liquid and solid phases, the general approach being similar to a previous investigation on bubbly flows (Shi and Rzehak, 2018). The focus of the work is put on the closures for all interfacial forces acting on particles, which differ significantly from those on bubbles, owing to the different interfacial conditions and deformability (Clift et al., 2005). Cases with low solid fractions, aka dilute suspensions, are considered, where other effects are negligible or at most of secondary importance. Apart from interest in its own right, results obtained for this restricted problem also provide a good starting point for the investigation of more complex situations including flows with moderate to high solids loading (Derksen, 2018), heat and mass transport or gas-solid-liquid three-phase flows (Kim and Kang, 1997). Meanwhile, results obtained should be applicable irrespective of large scale geometry and boundary conditions, as the same closures should work for all systems with same physics at particle scale.

The interfacial forces considered here include drag, lift, turbulent dispersion, and virtual mass. The importance of these forces may be summarized as follows. The drag force acts in opposition to the relative motion of a particle with respect to the surrounding fluid and is a key factor in determining the relative velocity of the particles. Virtual mass and turbulent dispersion account for, respectively, the inertia due particle accelerating or decelerating and the interphase turbulent momentum transfer, both of which are likely to be pronounced due to the unsteadiness inherent in stirred-tank flows. The lift force acts perpendicular to both the relative motion and the fluid vorticity. For particles translating within and in parallel to a unidirectional flow the role of lift force is to produce a lateral migration of the particles (Leal, 1980). In Poiseuille flows (either axisymmetric or plane), depending on the flow conditions, the resulting radial profile of solid fraction can peak either near

the wall or near the center line. In stirred tank flow, which are highly inhomogeneous, it is difficult to estimate the role of lift force a priori. The ratio between lift and drag may be evaluated from particle tracking simulations (Derksen, 2003, 2012) as $0.2\sqrt{Re_\omega}$ (with Re_ω denoting the shear Reynolds number) indicating a non-negligible lift unless Re_ω is vanishingly small.

The paper is organized as follows. In the next section a literature overview of numerical and experimental studies on particulate flows in stirred tanks is given. Section 3 presents all models that are used in this work. Section 4 discusses the selection of test cases from the survey of experiments in section 2 and the numerical issues concerning the present simulations. Section 5 presents the main results, i.e. an assessment of several model variants in comparison with the selected test cases. Conclusions and remarks are given in section 6.

2 LITERATURE REVIEW

2.1 Review of simulation studies

Table 1 gives an overview of simulation studies on solid-liquid flow in stirred tanks. Selection of works is based on the following criteria (Shi and Rzehak, 2018): Only works adopting the full Euler-Euler (E-E) or Euler-Lagrange (E-L) frameworks to couple the two-phase flows are taken. Also only works that validate their results by comparison with local measurements are considered. Lastly, for works from each group only the most recent one is listed. As may be seen, in addition to the basic multiphase framework, different modeling options have been chosen concerning turbulence modeling, interfacial forces taken into account, modeling of turbulent dispersion, description of particle-particle interaction, and lastly treatment of impeller rotation.

The two frameworks, namely E-E and E-L, differ in the way in which the solid flow is described. In the E-E framework, the solid phase is treated as a continuum with properties analogous to those of a fluid and governed by continuum forms of mass and momentum balance equations. In the E-L framework, particles are tracked individually or as clusters (when the solid fraction is high) based on Newton's second law. The advantage of E-L compared with E-E is that phenomena on the particle scale, such as collisions and particle-fluid interactions, can be represented with greater accuracy. On the other hand, the E-E framework is computationally more efficient for very large systems.

Concerning turbulence, the most fundamental approach is direct numerical simulation (DNS). However, this approach is still unfeasible for turbulent flows at industrial scale (Derksen 2012, 2018). Two more common approaches are Reynolds averaged Navier-Stokes (RANS) models and large eddy simulation (LES). RANS models can be further divided into two approaches: Reynolds stress models (RSMs) and two-equation eddy-viscosity models. According to Table 1, the latter have been used almost exclusively to study solid-liquid flow in stirred tanks. Due to its assumption of isotropic turbulence this approach generally shows good agreement with the measured data for the mean velocity in the bulk region but fails to predict the flow in regions with strong anisotropy (e.g. the near-impeller region). This limitation may be overcome by anisotropic models such as RSMs. Comparisons between RANS and LES have been performed for both single- and (solid-liquid) two-phase flows (Murthy and Joshi 2008, Guha et al., 2008). From these comparisons the conclusion emerges that, while LES provides improved predictions for single phase flow compared with RANS models, the improvement achieved by LES in two-phase flow predictions is still limited by the models used to couple the phases.

For the E-E framework, the turbulence model for the dispersed phase can be dealt with in three basic ways. These are the dispersed model, the mixture model, and the phasic model. The first two use only a single set of equations for, respectively, the continuous phase or the mixture, while the last uses two sets of equations, one for each of the phases. For details we refer to Yang and Mao (2014, section 3.4.3). It should be noted that implementation of the mixture model requires the wall boundary conditions for both phases to be identical. This is physically unreasonable since a viscous fluid cannot slip on the wall while for particles this is typically the case. Notwithstanding, comparisons of alternative approaches (Montante and Magelli, 2005; Fletcher and Brown, 2009; Wadnerkar et al., 2016) have concluded that, for solid fractions below 10%, all three models lead to similar results. Since the phasic model is computationally more expensive, the mixture and the dispersed models are more commonly used as indicated in Table 1.

For particulate flows, in addition to the shear-induced turbulence, it is sometimes necessary to take an additional particle-induced turbulence (PIT) into account. According to Table 1, the PIT has mostly been neglected in previous simulations of particulate flow in stirred tanks. In the few works taking it into account two approaches were used. The simpler one is to just add an extra particle-induced contribution to the effective viscosity following Sato et al (1981). To model the PIT effects on TKE and dissipation, additional source terms are introduced directly in the turbulence model equations (Kataoka and Serizawa, 1989).

Choice of the particle forces is yet another modeling decision to be made. Among these forces, drag has been assumed to be dominant whereas non-drag forces are often neglected in the works quoted in Table 1. Many correlations for drag force estimation are found in the literature, which are based on particles translating in stagnant liquid (see Loth (2008) for a review). In the highly turbulent flows occurring in stirred tanks, however, it has proven necessary to include the effect of turbulence on the drag force. Models that have been used frequently to account this effect are reviewed in Shah et al. (2015). For works that do take the non-drag forces into account, virtual mass and lift have been frequently considered, while the wall force has been mostly neglected. The virtual mass coefficient is always taken as 0.5, a value that has so far been confirmed to be reliable for dilute systems both numerically and experimentally (see Michaelides and Roig (2011) and references therein). As for the lift, often a positive constant coefficient $C_{\mathrm{L}} = 0.5$ was used (Ljungqvist and Rasmuson, 2001; Ochieng and Lewis, 2006; Guha et al., 2008; Fletcher and Brown, 2009). This value is valid for spheres with a free-slip surface in high-Reynolds-number flow but likely not be applicable for solid particles with no-slip surfaces, since the associated lift-generation mechanisms are fundamentally different (Legendre and Magnaudet, 1998).

For particulate flows, an important mechanism governing the distribution of particles is the turbulent dispersion, i.e. the transport of the particles by the turbulent eddies. For the E-L framework, this requires the estimation of the instantaneous fluid velocity along the particle trajectory, which is typically modeled by various stochastic approaches (Derksen, 2003; Sommerfeld et al., 2008, section 4.3.3). For the E-E framework, two different approaches are used. In the first, the solid phase continuity equation is augmented by a diffusive term to a convection-diffusion equation (CDE) (see e.g. Loth (2001)). As seen from Table 1, this method has been used quite often. However, there are a significant number of theoretical works which have shown that this simplification might be questionable (Simonin, 1990; Reeks, 1991; Crowe et al., 1996; Drew, 2001; Sommerfeld et al., 2008, section 4.4.1). Most of those authors conclude that the essence of dispersion should appear as a force in the momentum equation. So far various formulations regarding this turbulent dispersion force have been proposed, among which the Farve-averaged-

drag model (FAD, Burns et al., 2004) and the kinetic theory based model (Reeks, 1991; de Bertodano, 1998) found numerous applications to particulate flow in stirred tanks (Ljungqvist and Rasmuson, 2001; Ochieng and Lewis, 2006; Fletcher and Brown, 2009; Qi et al., 2013; Maluta et al. (2019)).

If the system is not dilute particle dispersion is not only caused by turbulence, but in addition also due to particle-particle collisions. In the E-L framework, this has been dealt with by various collision models (Derksen, 2003, 2012, 2018). In the E-E framework, the effect of collisions is included by the kinetic theory of granular flows (KTGF, Gidaspow, 1994), which treats momentum and energy transfer due particle-particle collisions in the particulate flow in an analogous way as that for molecules in a single-phase gas. Compared with the various collision models used in the E-L framework, the significant advantage of the KTGF approach is that there is no need to consider the mechanical interaction of individual particles so larger systems can be modeled. However, the constitutive equations needed for the KTGF approach are largely based on empiricism. The problem of deriving these constitutive equations from more basic physical principles has not yet been solved and remains a significant challenge for the future.

Finally, modeling the flow inside baffled stirred tanks requires suitable boundary conditions for the impeller blades and the disc on which they are mounted, because these sections are moving relative to the fixed baffles and the tank wall. Different impeller-rotation models have been thoroughly described by Yang and Mao (2014, section 3.2.5). We here just note that the most frequently used approaches include the impeller boundary condition (IBC), sliding mesh/grid (SG), inner-outer approach (IO), and multiple reference frame (MRF). Comparisons of alternative modeling approaches have been conducted by Brucato et al. (1998a) and more recently by Shi and Rzehak (2018). From these comparisons, the MRF has emerged as reliable and considerably more efficient computationally.

Table 1: Simulations of solid-liquid flow in stirred tanks.

Reference	Data source	Multi-phase approach	Turbulence / PIT	Interface forces	Turbulent dispersion	Particle-particle collision	Impeller rotation *)
Kohnen (2000)	Kohnen (2000)	E-E	dispersed k-ε / none	F^{drag}	none	KTGF	SG
Ljungqvist & Rasmuson (2001)	Ljungqvist & Rasmuson (2004)	E-E	phasic k-ε / none	F^{drag}, F^{lift}, F^{VM}	none / force	none	IBC
Oshinowo & Bakker (2002)	Godfrey & Zhu (1994), Guiraud et al. (1997)	E-E	dispersed k-ε / none	F^{drag}	none	KTGF	IBC
Wang et al. (2003)	Nouri & Whitelaw (1992), Yamazaki et al. (1986)	E-E	dispersed k-ε / source terms	F^{drag}	CDE	none	IO
Khopkar et al. (2006)	Yamazaki et al. (1986), Godfrey & Zhu (1994)	E-E	mixture k-ε / none	F^{drag}	CDE	none	MRF

Montante & Magelli (2007)	Montante & Magelli (2007)	E-E	mixture k-ε / none	F^{drag}	CDE	none	SG
Guha et al. (2008)	Guha et al. (2007)	E-E	mixture k-ε / none	F^{drag}, F^{lift}, F^{VM}	force	KTGF	MRF
		E-L	LES / none		stochastic tracking	included	IBC
Kasat et al. (2008)	Yamazaki et al. (1986)	E-E	mixture k-ε / none	F^{drag}	force	none	MRF
Ochieng & Onyango (2008)	Ochieng & Lewis (2006)	E-E	dispersed k-ε / Sato	F^{drag}, F^{lift}, F^{VM}, F^{wall}	force	KTGF	SG
Shan et al. (2008)	Shan et al. (2008)	E-E	dispersed k-ε / source terms	F^{drag}	none	none	IBC
Sardeshpande et al. (2011)	Sardeshpande et al. (2011)	E-E	mixture k-ε / none	F^{drag}	force	none	MRF
Feng et al. (2012)	Yamazaki et al. (1986), Micheletti et al. (2003, 2004), Guha et al. (2007), Montante et al. (2012)	E-E	dispersed k-ε & RSM / source terms	F^{drag}	force	none	IO
Liu & Barigou (2014)	Liu & Barigou (2014)	E-E	mixture k-ε / none	F^{drag}	none	none	MRF
Tamburini et al. (2014)	Micheletti et al. (2003)	E-E	dispersed & mixture k-ε / none	F^{drag}	force / CDE	none	MRF / SG
Wadnerkar et al. (2016)	Guida et al. (2010)	E-E	dispersed, mixture, and phasic k-ε & RSM / none	F^{drag}	force	none / KTGF	MRF
Wang et al. (2017)	Pianko-Oprych et al. (2009)	E-E	dispersed k-ε / none	F^{drag}, F^{VM}	none	KTGF	MRF
Li et al. (2018)	Li et al. (2018)	E-L	DNS	F^{drag}	resolved	included	IBC
Maluta et al. (2019)	Carletti et al. (2014)	E-E	mixture k-ε & RSM	F^{drag}, F^{lift}	force	none / KTGF	MRF

*) IO, inner–outer method; SG, sliding grid/mesh; IBC, impeller boundary condition; MRF, multiple reference frame. Other items: CDE, convection diffusion equation; RSM, Reynolds stress model; KTGF, kinetic theory of granular flows. Further explanations are given in the text.

2.2 Review of experimental studies

An overview of previously reported experimental studies on solid-liquid flow in mechanically stirred tanks is shown in Table 2. The focus is on works that provide measurements of spatially resolved data for monodisperse suspensions. Finally, for measurements conducted by the same group and employing identical techniques, only the most recent work is listed. Exceptions to this last rule are works that have been used for comparison in the simulation studies above.

For most of the experimental studies, a single standard Rushton turbine or pitched blade turbine rotating with roughly 200 to 1200 rpm is used, the tank diameter is in the range of 100 to 500 mm and the ratio of fill height to diameter is close to one. For works using multiple impellers (Magelli et al., 1990; Montante et al., 2002; Montante and Magelli, 2007), the aspect ratio is increased in proportion. Bigger tanks are considered by Spidla et al. (2005) and Angst and Kraume (2006), smaller ones by Gabriele et al. (2011).

Most works listed in Table 2 focus on the so-called complete suspension condition (i.e. conditions with an impeller rotation speed much higher than the just-suspension speed (see Guha et al. (2007) and references therein)). Cases with incomplete suspension are also investigated in Nouri and Whitelaw (1992), Micheletti et al. (2003), Tamburini et al. (2013), and Carletti et al. (2014). The glass-water system with a solid-to-liquid density ratio of ≈ 2.5 has been investigated quite often. For lower density ratios, polystyrene or polymethylmethacrylate (PMMA, e.g. Diakon™) particles were used (Magelli et al., 1990; Nouri and Whitelaw, 1992; Micheletti et al., 2003, 2004; Montante and Magelli, 2007; Gabriele et al., 2011; Sardeshpande et al., 2011) while higher density ratios are obtained for bronze (Magelli et al., 1990; Montante and Magelli, 2007) or nickel particles (Ljungqvist and Rasmuson, 2004; Ochieng and Lewis, 2006). Various aqueous solutions with identical refractive index as that of the suspended solid phase are sometimes selected as the working fluid, while their densities are always comparable to that of water. The investigated mean (volumetric) solid fraction spans a wide range of 0.1% to 30%. Significantly lower solid loadings are considered by Ljungqvist and Rasmuson (2004, 0.01%) and Tamburini et al. (2013, $< 0.01\%$), respectively. The particle diameter is mostly in the range of 0.1 to 1 mm. Coarser particles are considered by Gabriele et al. (2011, 1.5 mm), Pianko-Oprych et al. (2009, 3 mm), Guida et al. (2010, 3 mm), and Li et al. (2018, 8 mm).

As for the data, an ideal data set that contains all relevant observables (i.e. phase mean and fluctuation velocities as well as solid fraction) with high spatial resolution and profiles along several directions at several positions is available so far only from the data sets of Nouri and Whitelaw (1992) and Unadkat et al. (2009). However, the image analysis method used by Unadkat et al. (2009) might not be reliable (Tamburini et al., 2013) and the resulting fraction maps obtained should be interpreted as an indication only. Some relatively comprehensive data sets, e.g. Guiraud et al. (1997), Ochieng and Lewis (2006), and Chen et al. (2011), employed complex-shaped impellers whose geometry is unfortunately not fully specified. Besides, although the experiment of Nouri and Whitelaw (1992) considered varying values of density ratio, mean solid fraction, and particle diameter only one data set provides the information of both mean velocity and local solid fraction (see Table 6 for the details). Thus to achieve a solid validation, a combination of several data sets seems necessary.

Measurement methods are partly intrusive using various well-known probe techniques, like electrical and optical needle probes (denoted as IP and OP in Table 2), for solid fraction. Photographic methods to determine solid fraction by image analysis (IA) have been adapted for

use in stirred tanks using either backlighting (Magelli et al., 1990) or laser light sheets (Unadkat et al., 2009; Tamburini et al., 2013). Methods like PIV, LDA, and PDA can readily be used to measure particle velocity and by adding tracer particles also liquid velocity. These optical techniques are non-intrusive but limited to suspensions with low solids loading. This drawback can be overcome by matching the refractive index of the liquid to that of the dispersed phase (RIM) as several works in Table 2 have shown. More sophisticated techniques that allow non-intrusive probing of opaque suspensions are radioactive particle tracking techniques including CARPT and PEPT. Both resolve directly Lagrangian particle trajectories while the Eulerian information like phase velocity and fraction is obtained by applying appropriate reconstructing algorithms. More advanced tomographic methods such as electrical resistance tomography (ERT) and ultrasound velocity profiling (UVP) are just about beginning to be applied to this field.

Table 2: Experiments on solid-liquid flow in stirred tanks.

Reference	Tank diameter / Fill height (mm)	Impeller type *) / Diameter / Bottom clearance (mm)	Density ratio / Solid fraction (*v*/*v* %) / Particle diameter (mm)	Rotation rate (rpm)	Technique **)	Measured quantities
Yamazaki et al. (1986)	300 / 300	RT / 70 / 90	2.37 - 2.62 / 5, 20 / 0.087 - 0.23	300 - 1200	OP	$\bar{\alpha}_S$
Magelli et al. (1990)	43.5 / 174	4×RT / 14.5 / 21.8	1.02-8.41 / ~ 7.5 / 0.14 - 0.98	302 - 1008	IA	$\bar{\alpha}_S$
	78.7 / 315	4×RT / 26.2 / 39.4				
Nouri & Whitelaw (1992)	294 / 294	RT / 98, 147 / 73.5, 98	1.18 - 2.95 / 0, 0.02 - 2.5 / 0.23 - 0.67	150 - 313	LDA & RIM	$\bar{u}_L$, u'_L, $\bar{u}_S$, u'_S, $\bar{\alpha}_S$
Godfrey & Zhu (1994)	154 / 154	PBT / 51 / 46	2.26 / 0.4 - 30 / 0.23 - 0.67	600 - 1600	RIM	$\bar{\alpha}_S$
Guiraud et al. (1997)	300 / 300	M-TT / 140 / 100	2.23 / 0, 0.5 / 0.25	306	PDA	$\bar{u}_L$, u'_L, $\bar{u}_S$, u'_S
Kohnen (2000)	220 / 220	RT / 94 / 73.3	~ 2.5 / 0, 5, 10 / 0.55	650	LDA & RIM	$\bar{u}_L$, u'_L
Montante et al. (2002)	230 / 920	4×PBT / 94 / 115	2.45 / 0.12 -0.41 / 0.13 - 0.79	486 - 1200	OP	$\bar{\alpha}_S$
	480 / 1440	3×PBT / 195 / 240				
Micheletti et al. (2003)	290 / 290	RT / 98 / 43.5-96.6	1.05 - 2.47 / 0, 1.8 - 15.5 / 0.15 - 0.71	100 - 1200	IP	$\bar{\alpha}_S$
Ljungqvist & Rasmuson (2004)	297 / 297	PBT / 99 / 99	2.45 – 8.9 / 0, ~ 0.01 / 0.14 - 0.45	180 - 540	PDA	$\bar{u}_L$, $\bar{u}_S$
Micheletti & Yianneskis (2004)	80.5 / 80.5	RT / 27 / 27	1 / 0, 0.1 - 2.0 / 0.19	2500	LDA & RIM	$\bar{u}_L$, u'_L
Spidla et al. (2005)	1000 / 1000	PBT / 333 / 167, 333	2.5 / 5, 10 / 0.14, 0.35	156 - 267	IP	$\bar{\alpha}_S$
Angst & Kraume (2006)	200 / 200	PBT 62.5 / 62.5	2.5 / 2 - 10 / 0.2	678, 877	OP	$\bar{\alpha}_S$
	400 / 400	PBT 125 / 125		419, 538		
	900 / 900	PBT 281 / 281		275		
Ochieng & Lewis (2006)	380 / 380	M-HA / 126.7 / 57	8.9 / 0, 0.03 - 2 / 0.15 - 1.0	200 - 500	LDA & IA	$\bar{u}_L$, $\bar{\alpha}_S$
Montante & Magelli (2007)	232 / 928	4×RT / 79 / 116	1.15, 2.46 / 0.05 - 0.15 / 0.33	1146, 1457	PIV & IA	$\bar{u}_L$, $\bar{\alpha}_S$
Guha et al. (2007)	200 / 200	RT / 66.7 / 66.7	2.5 / 1, 7 / 0.3	850 - 1200	CARPT	$\bar{u}_S$, u'_S
Virdung & Rasmuson (2007)	150 / 150	PBT / 50 / 50	2.5 / 0, 0.5 - 1.5 / 1.0	900	PIV& RIM	$\bar{u}_L$, $\bar{u}_S$
Shan et al. (2008)	300 / 420	PBT / 80 / 160	1.97 / 0.5 / 0.08	113 - 173	OP	$\bar{\alpha}_S$

Pianko-Oprych et al. (2009)	288 / 288	PBT / 144 / 72	2.16 / 0, 2.31 / 3.0	150 - 406	PEPT	$\bar{u}_L, \bar{u}_S$
Unadkat et al. (2009)	101 / 101	PBT / 33.7 / 25.25	2.5 / 0, 0.2 - 0.5 / 1.0	1600	PIV & IA	$\bar{u}_L, \bar{u}_S, u'_L, u'_S, \varepsilon_L, \bar{\alpha}_S$
Guida et al. (2010)	288 / 288	PBT / 144 / 72	2.16 / 0, 2.5 - 23.6 / 3.0	330 - 590	PEPT	$\bar{u}_L, \bar{u}_S, \bar{\alpha}_S$
Chen et al. (2011)	220 / 220	CBY / 139 / 55	2.50 / 0, 0.2 - 5.0 / 0.65	410	PIV& RIM	$\bar{u}_L, u'_L, \varepsilon_L$
Gabriele et al. (2011)	45 / 45	PBT / 24.5 / 15	1.38 / 0, 1.5, 5.0 / 1.5	900	PIV& RIM	$\bar{u}_L, u'_L, \varepsilon_L$
Sardeshpande et al. (2011)	700 / 700	PBT / 200 / 233	1.06, 2.5 / 1 - 7 / 0.25, 0.35	202 - 275	UVP	$\bar{u}_L, \bar{u}_S$
Harrison et al. (2012)	220 / 220	RT / 110 / 77.3	2.65 / 5, 10, 20 / 0.16, 0.51, 0.73	236, 547	ERT	$\bar{\alpha}_S$
Montante et al. (2012)	232 / 232	RT / 77.3 / 77.3	2.47 / 0, 0.05 - 0.20 / 0.12 - 0.77	852	PIV	$\bar{u}_L, u'_L$
Tamburini et al. (2013)	190 / 190	RT / 95 / 63.3	2.48, 3.45 / 0.006, 0.008 / 0.13, 0.5	300 - 600	IA	$\bar{\alpha}_S$
Carletti et al. (2014)	232 / 250	PBT / 78 / 78	2.5 / 9 - 15 / 0.13, 0.37	500 - 900	ERT	$\bar{\alpha}_S$
Gu et al. (2017)	480 / 800	PBT+RT / 200 / 160	2.47 / 5 / 0.12	60 - 380	Sampling	$\bar{\alpha}_S$
Li et al. (2018)	220 / 220	PBT / 158 / 44	1.63, 2.21 / 0, 1 - 8 / 8	450, 496	PIV& RIM	$\bar{u}_L, u'_L, \bar{\alpha}_S$

*) CBY, down-pumping 3-blade propeller; M-HA, Mixtec HA735 propeller; M-TT, Mixel TT propeller; PBT, pitched blade turbine; RT, Rushton turbine.

**) Intrusive: IP, impedance probe; OP, optical probe. Non-intrusive: CARPT, computer automated radioactive particle tracking; ERT, electrical resistance tomography; IA, image analysis; LDA, laser Doppler anemometry; PDA, phase-Doppler anemometry; PEPT, positron emission particle tracking; PIV, particle image velocimetry; RIM, refractive index matching; UVP, ultrasound velocity profiler.

2.3 Reynolds numbers and lengthscales

The review above facilitates to evaluate roughly the ranges of parameters that apply to solid suspensions in stirred tank flows covered in experiments. These include in particular various lengthscales, i.e. the particle size, the Kolmogorov lengthscale, and the typical size of the energy containing eddies, as well as the relative velocity between the particles and the liquid. From these, particle- and shear Reynolds numbers may be derived. Ranges of these parameters are important for the development of closure models of, especially, the interfacial forces.

The particle Reynolds number is defined as $Re_\mathrm{p} = d_\mathrm{p} u_\mathrm{rel}/\nu$, where d_p is the particle diameter, u_rel denotes the magnitude of relative velocity, and ν is the liquid kinematic viscosity. According to the experiments listed in Table 2, the glass-water system has been frequently considered. In this case the kinematic viscosity of the liquid ν is about 10^{-6} $\mathrm{m^2 s^{-1}}$. The ratio of the particle density ρ_S to that of the liquid phase ρ_L is around 2.5. The typical size of the particles considered is in the range $0.1\ \mathrm{mm} \leq d_\mathrm{p} \leq 1\ \mathrm{mm}$. The terminal settling velocity is most often used as a reference for the relative velocity. In the Stokes limit, the settling velocity is $d_\mathrm{p}^2 g(\rho_S - \rho_L)/(18\nu\rho_S)$ indicating $1 \leq Re_\mathrm{p} \leq 1000$. This estimation of Re_p can be improved by considering two aspects. On one hand, the finite Reynolds number effect is to increase the Stokes drag by a ratio of $\left(1 + 0.15\, Re_\mathrm{p}^{0.687}\right)$ (Schiller and Naumann, 1933) and thus to reduce the relative velocity. On the other hand, flow in a stirred tank is highly turbulent such that particle inertia significantly contribute

to the relative velocity. Previous simulation results (Derksen, 2003, 2012; Khopkar et al., 2006; Guha et al., 2008) indicate that the magnitude of relative velocity in the near impeller region is approximately 2 times that of the settling velocity. The combination of both aspects results in a somewhat narrower range of $1 \leq Re_{\mathrm{p}} \leq 800$.

The shear Reynolds number is defined as $Re_{\omega} = d_{\mathrm{p}}^2 \omega / \nu$ with ω denoting the magnitude of flow shear rate. In stirred tank flows, ω is proportional to the impeller rotation rate Ω (in $\mathrm{rev/s}$). CFD simulations (Derksen and Van den Akker, 1998; Derksen, 2003) indicate that ω easily exceeds 10Ω in the near impeller region, which can be taken as an upper estimate. According to Table 2, Ω has a magnitude around 10 which gives a range of $0 < Re_{\omega} \leq 100$.

The Kolmogorov lengthscale η for stirred tank flows with fully developed turbulence can be estimated empirically (Derksen, 2003, 2012) as $\eta = D_{\mathrm{i}} Re_{\mathrm{i}}^{-0.75}$, where D_{i} is the impeller diameter and $Re_{\mathrm{i}} = \Omega d_{\mathrm{i}}^2 / \nu$ denotes the impeller Reynolds number. According to Table 2, the impeller Reynolds number is around 5×10^4, and the impeller diameter is around 0.1 m. Thus η has a magnitude of $O(10^{-2})$ mm which agrees with values estimated in DNS studies (Gillissen and Van den Akker, 2012; Derksen, 2012). On the other hand, the Eulerian longitudinal integral lengthscale Λ, which is a measure of the energy-containing eddies, should be about the same order of magnitude as turbulence-generating sources. For stirred tank flows, the impeller blade was suggested to be the major turbulence source (Wu and Patterson, 1989). The typical size of the impeller blade is $1/15 \sim 1/12$ that of the tank diameter thus Λ has a magnitude of $O(10^1)$ mm.

3 OVERVIEW OF MODELS

This section describes the simulation models employed. Section 3.1 briefly summarizes the basic conservation equations of the E-E framework, which is applied in the present work. Since various particle forces are known from previous works to have an effect on the accuracy of the model predictions, an attempt is made here to assemble a rather complete description of these forces, which is detailed in section 3.2. Section 3.3 discusses effects of liquid phase turbulence on the particles which comprise a modification of the drag force due to turbulence and the modeling of turbulent dispersion. The modeling of turbulence in the liquid phase is based on the Reynolds stress model proposed by Speziale, Sarkar, and Gatski (Speziale et al., 1991, hereafter referred to as SSG RSM), which has been used successfully in previous work and is described in section 3.4. Comparisons of different RANS models for stirred tank simulations are provided for example in Ciofalo et al. (1996), Cokljat et al. (2006), Murthy and Joshi (2008), Feng et al. (2012), Morsbach (2016), Wadnerkar et al. (2016), and Shi and Rzehak (2018).

3.1 Euler-Euler framework for solid-liquid flow

Using the index $k = L, S$ to denote the liquid and solid phase, respectively, the phasic continuity and Navier–Stokes equations take the form (Drew and Passman, 2006)

$$\frac{\partial}{\partial t}(\alpha_k \rho_k) + \nabla \cdot (\alpha_k \rho_k \boldsymbol{u}_k) = 0 \tag{1}$$

and

$$\frac{\partial}{\partial t}(\alpha_\kappa \rho_\kappa \boldsymbol{u}_\kappa) + \nabla \cdot (\alpha_\kappa \rho_\kappa \boldsymbol{u}_\kappa \otimes \boldsymbol{u}_\kappa) = \tag{2}$$

$$-\alpha_k \nabla p_k + \nabla \cdot \left(2\alpha_k \, \mu_k^{\mathrm{mol}} \mathbf{D}_k\right) - \nabla \cdot (\alpha_k \rho_k \mathbf{R}_k) + \boldsymbol{F}_k^{\mathrm{body}} + \boldsymbol{F}_k^{\mathrm{inter}}.$$

In Eq. (2), α is the volume fraction, p denotes the pressure, $\mathbf{D} = (\nabla \boldsymbol{u} + (\nabla \boldsymbol{u})^{\boldsymbol{T}})/2$ is the strain rate tensor, and μ^{mol} is the molecular dynamic viscosity. μ_S^{mol} is assumed to be identical with μ_L^{mol}, an assumption that was made in most simulation studies listed in Table 1. $\mathbf{R}$ is the Reynolds stress tensor which is defined in terms of the turbulent fluctuating velocities $\boldsymbol{u}_k'$ as $\mathbf{R}_k = \langle \boldsymbol{u}_k' \otimes \boldsymbol{u}_k' \rangle$, where $\langle \quad \rangle$ makes the involved averaging operation explicit. $\mathbf{R}_L$ is obtained by directly solving a transport equation as discussed in detail in section 3.4 while $\mathbf{R}_S$ is presently neglected.

The body forces $\boldsymbol{F}_k^{\mathrm{body}}$ comprises the gravity force as well as centrifugal and Coriolis forces where a rotating frame of reference is adopted.

The term $\boldsymbol{F}_k^{\mathrm{inter}}$ accounts for the momentum transfer between the phases. Due to momentum conservation the relation $\boldsymbol{F}_S^{\mathrm{inter}} = -\boldsymbol{F}_L^{\mathrm{inter}}$ holds. This term comprises of a number of contributions and the corresponding models employed here are summarized in Table 3. A detailed discussion thereof will be given in sections 3.2 and 3.3.

Table 3: Summary of particle force correlations.

force	reference
drag	Schiller and Naumann (1933) with modification due to turbulence discussed in section 3.3.2
lift	Shi and Rzehak (2019)
turbulent dispersion	de Bertodano (1998) with turbulence scales discussed in section 3.3.1
virtual mass	constant coefficient $C_{\mathrm{VM}} = 1/2$

3.2 Interfacial forces

Interfacial forces considered include drag, lift, virtual mass, and turbulent dispersion. Although the last one has been frequently classified as an interfacial force, its description is deferred to section 3.3.3, because it depends on turbulence parameters that are naturally introduced only in section 3.3.1. For flow in the near wall region there could be additional wall effects, e.g. an enhancement of drag (Sommerfeld et al., 2008, section 3.1) or a suppression of shear-lift (Shi and Rzehak, 2020). Moreover, the presence of the wall introduces a wall-lift force directed away from the wall (Shi and Rzehak, 2020). These wall effects are important for modeling multiphase flows in rather confined geometries but are neglected in the present study as the near-wall region occupies only a small portion of the stirred tank volume.

3.2.1 Drag force

The drag force acting on the dispersed phase takes the form

$$\boldsymbol{F}_S^{\mathrm{drag}} = -C_{\mathrm{D}} \frac{3}{4} d_{\mathrm{p}}^{-1} \rho_L \alpha_S u_{\mathrm{rel}} \boldsymbol{u}_{\mathrm{rel}}, \tag{3}$$

where $\boldsymbol{u}_{\mathrm{rel}} = \boldsymbol{u}_S - \boldsymbol{u}_L$ denotes the relative velocity and C_{D} is the drag coefficient. For solid spheres translating in a stagnant fluid, the drag correlation of Schiller and Naumann (1933) applies:

$$C_{\mathrm{D},0} = \frac{24}{Re_{\mathrm{p}}}\left(1 + 0.15\, Re_{\mathrm{p}}^{0.687}\right). \tag{4}$$

3.2.2 Lift force

The lift force acting on the dispersed phase takes the form

$$\boldsymbol{F}_S^{\text{lift}} = C_{\text{L}}\alpha_S\rho_L\boldsymbol{\omega}_L \times \boldsymbol{u}_{\text{rel}}, \tag{5}$$

where $\boldsymbol{\omega}_L$ gives the vorticity of the fluid with $\boldsymbol{\omega}_L \equiv \nabla \times \boldsymbol{u}_L$, and C_{L} is the lift coefficient. The lift force for spherical particles rotating freely only under the action of the surrounding fluid with no external torque applied is frequently described by a linear combination of contributions from flow vorticity and particle rotation (Shi and Rzehak, 2019), i.e.

$$C_{\text{L}} = C_{\text{L}\omega} + \frac{3}{8} f_{\omega-\Omega} C_{\text{L}\Omega}, \tag{6}$$

where $C_{\text{L}\omega}$ and $C_{\text{L}\Omega}$ denote the coefficients of the vorticity- and rotation-induced lift forces, respectively. $f_{\omega-\Omega}$ is the dimensionless vorticity-induced rotation rate defined by $f_{\omega-\Omega} \equiv 2\Omega_{fr}/\omega$, where Ω_{fr} denotes the vorticity-induced particle rotation rate in the torque-free condition.

According to the review of Shi and Rzehak (2019) the two lift coefficients take the form:

$$C_{\text{L}\omega} = \begin{cases} \dfrac{27}{2\pi^2}\left(SrRe_{\text{p}}\right)^{-1/2} J(\epsilon) - \dfrac{33}{32}\exp\left(-0.5\,Re_{\text{p}}\right) & \text{for } Re_{\text{p}} \le 50 \\ -0.048Sr^{-1}\exp(0.525Sr)\left\{0.49 + 0.51\tanh\left[5\lg\left(\dfrac{Re_{\text{p}}Sr^{0.08}}{120}\right)\right]\right\} & \text{for } Re_{\text{p}} > 50 \end{cases} \tag{7}$$

and

$$C_{\text{L}\Omega} = 1 - 0.62\tanh\left(0.3Re_{\text{p}}^{1/2}\right) - 0.24\tanh\left(0.01Re_{\text{p}}\right)\coth(0.8Rr^{0.5})\arctan[0.47(Rr-1)], \tag{8}$$

where Sr and Rr denote, respectively, the dimensionless flow vorticity with $Sr = \omega d_{\text{p}}/u_{\text{rel}}$ and the dimensionless particle rotation rate with $Rr = {}_{fr}d_{\text{p}}/u_{\text{rel}}$, $J(\epsilon)$ is the function defined by McLaughlin (1991, Eq. (20)), and ϵ is a lengthscale ratio defined by $\epsilon = \sqrt{Sr/Re_{\text{p}}}$. An appropriate correlation for $J(\epsilon)$ was proposed by Legendre and Magnaudet (1998) as

$$J(\epsilon) = 2.255(1 + 0.20\epsilon^{-2})^{-3/2}. \tag{9}$$

$f_{\omega-\Omega}$ in Eq. (6) is related to the particle- and shear Reynolds numbers via (Shi and Rzehak, 2019)

$$f_{\omega-\Omega} = \{1 + 0.4[\exp(-0.0135Re_{\omega}) - 1]\}\left(1 - 0.07026Re_{\text{p}}^{0.455}\right). \tag{10}$$

Eqs. (5) - (10) summarize the lift force correlation proposed by Shi and Rzehak (2019) concerning solid particles translating in stream-wise linear shear flows under torque-free conditions. Its advantage over the older correlation of Mei (1992), which has been widely used in engineering, lies in two aspects. Firstly it accounts for the contributions from flow vorticity and particle rotation simultaneously while the correlation in Mei (1992) accounts for the former only. DNS studies have shown the necessity to consider the (torque-free) rotation-induced lift when $Re_{\text{p}} \ge 5$. Secondly, the correlation in Mei (1992) neglects negative values of $C_{\text{L}\omega}$, which have been revealed in DNS studies beyond $Re_{\text{p}} = 50$. This effect is taken into account in the correlation from Shi and Rzehak (2019). These advantages motivate application of the correlation of Shi and Rzehak (2019) to describe the lift force.

3.2.3 Virtual mass force

The virtual mass force acting on the dispersed phase takes the form

$$\boldsymbol{F}_S^{\mathrm{VM}} = C_{\mathrm{VM}}\alpha_S\rho_L\left(\frac{D_L\boldsymbol{u}_L}{Dt} - \frac{D_S\boldsymbol{u}_S}{Dt}\right), \tag{11}$$

where D_L/Dt and D_S/Dt denote material derivatives with respect to the liquid and solid velocities, respectively. For the virtual mass coefficient a value of $C_{\mathrm{VM}} = 0.5$ is applied.

3.3 Turbulence effects

This section discusses the turbulence effects on the interfacial forces. Since most of the turbulence-particle interactions are depend on the particle-turbulence interaction timescale, this quantity is discussed first. Modeling of the drag modification and turbulent dispersion force are then discussed.

3.3.1 Particle-turbulence interaction timescale

The particle-turbulence interaction timescale T_{L}^S is a crucial parameter in describing turbulence effects on the motion of the dispersed phase (Balachandar and Eaton, 2010). A simple form of this timescale (Loth, 2001) accounting for the crossing-trajectories effect (Yudine, 1959) is composed of the Lagrangian integral timescale following the fluid motion, T_{L}^L, and the time for a particle to cross an typical eddy, τ_{cross}, as:

$$T_{\mathrm{L}}^S \approx \left({T_{\mathrm{L}}^L}^{-2} + \tau_{\mathrm{cross}}^{-2}\right)^{-\frac{1}{2}}. \tag{12}$$

This simple form neglects the continuity effect (Csanady, 1963), accounting for which however would make it necessary to describe T_{L}^S in tensor form. To avoid this complication here as well as in the modeling of turbulent dispersion, the scalar form Eq. (12) is employed presently as a basic description. The two timescales are defined in terms of quantities that can be computed from a RANS turbulence model as

$$T_{\mathrm{L}}^L = C_T\frac{k}{\varepsilon}$$
$$\tau_{\mathrm{cross}} = \frac{\Lambda}{u_{\mathrm{rel}}} = C_\Lambda\frac{k^{3/2}}{u_{\mathrm{rel}}\,\varepsilon}\quad, \tag{13a, b}$$

where Λ denotes the Eulerian longitudinal integral lengthscale and $u_{\mathrm{rel}} = |u_S - u_L|$ the relative velocity. The constants C_T and C_Λ are discussed in the following.

According to the cornerstone dissipation scaling of turbulence, sometimes referred to as Kolmogorov's zeroth law (Pearson et al., 2004),

$$\Lambda = C_\varepsilon\frac{(2/3\,k)^{3/2}}{\varepsilon}. \tag{14}$$

Here C_ε is a constant which is expected to be universal in the limit of high Reynolds numbers. While the verification of this assertion and the determination of the numerical value of C_ε is still an active subject of research, quite a few studies (reviewed by Ishihara et al. (2009)) have shown that $C_\varepsilon \approx 0.43$ for simulations of statistically stationary forced turbulence in a periodic box. The same value has also been obtained by Pope (2000, sect. 6.5.7) from a model for the turbulent energy

spectrum. Using this value in Eq. (14) and comparing with Eq. (13b) gives $C_\Lambda \approx 0.234$. In the present work, this value will be used since at least it is well-established for a well-defined idealization. In the absence of clear and unambiguous results for more realistic situations this provides the best available starting point, on which future improvements may be based. However, it has to be acknowledged that the value of C_ε depends on initial and boundary conditions (Vassilicos, 2015), e.g. twice as high values are often found experimentally in grid-generated turbulence. Values assumed for C_Λ in previous studies of particulate flows, often with little to no further justification, range between 0.09 and 0.54 (see Table 4).

Results concerning T_L^L are mostly presented in terms of the dimensionless parameter

$$\beta = \frac{T_\mathrm{L}^L\,(2/3\,k)^{1/2}}{\Lambda} = T_\mathrm{L}^L \frac{(2/3)^{1/2}}{\mathrm{C}_\Lambda}\frac{\varepsilon}{k}, \tag{15}$$

by virtue of Eq. (13b). Solving for T_L identifies

$$C_T = \frac{\mathrm{C}_\Lambda}{(2/3)^{1/2}}\beta \approx 0.287\beta \tag{16}$$

using the value of C_Λ from above. Simulations of statistically stationary forced turbulence in a periodic box give an asymptotic value of $\beta \approx 0.78$ at large Reynolds numbers (Yeung et al., 2001; Sawford et al., 2008; Sawford and Yeung, 2011), which corresponds to $C_T \approx 0.224$. Like above, this well-defined value will be used as a starting point in the present work. Again it has to be acknowledged that experiments on grid turbulence often show values of β as low as half of the one used here. Values for C_T assumed in previous studies of particulate flows are given in Table 4, from which a wide spread of values ranging from 0.09 to 0.5 becomes obvious. Thus, a systematic study of the influence of different choices seems appropriate.

Table 4: Values of C_T and C_Λ used in previous studies.

reference	C_T†	C_Λ	β
Snyder and Lumley (1971)	-	-	~0.92
Tennekes and Lumley (1971, Eq. (8.5.15))	-	-	$2/3 = 0.67$
Shlien and Corrsin (1974, $R_\lambda \approx 70$)	-	-	1
Calabrese and Middleman (1979)	0.41	-	-
Boysan et al. (1982)	$0.5 \times 2^{-1/2} C_\mu^{3/4} = 0.058$	-	-
Gosman and Loannides (1983)	-	$C_\mu^{1/2} = 0.3$	-
Pourahmadi and Humphrey (1983)	0.41	-	-
Shuen et al. (1983)	$0.5 \times (3/2)^{1/2} C_\mu^{3/4} = 0.101$	$C_\mu^{3/4} = 0.164$	-
Chen and Wood (1984)	$C_\mu^{3/4} = 0.164$	$C_\mu^{3/4} = 0.164$	-

† Note that the relation between the "eddy life-time", which has been frequently referred to in references listed in Table 4, and the Lagrangian intergral time scale T_L^L depends on the functional shape of the Lagrangian velocity correlation coefficient (see Gouesbet and Berlemont (1999) for details).

Mostafa and Mongia (1987)	$(3/2)^{1/2}C_\mu^{3/4} = 0.201$	$C_\mu^{3/4} = 0.164$	1
Sato and Yamamoto (1987, $R_\lambda = 70$)	-	-	0.3 - 0.6
Amsden et al. (1989, page 17)	0.50	$C_\mu^{3/4} = 0.164$	-
Simonin and Viollet (1990)	$(3/2)^{1/2}C_\mu = 0.110$	$(3/2)^{1/2}C_\mu = 0.110$	-
Zhou and Leschziner (1991)	$0.8 \times (3/2)^{1/2}C_\mu^{3/4} = 0.161$	-	
Lu (1995)	-	$(0.212/0.36) \times (3/2)^{1/2} = 0.32$	0.36
de Bertodano (1998)	$C_\mu^{3/4} = 0.164$	$1/2\, C_\mu^{1/4} = 0.274$	-
Peirano and Leckner (1998)	$C_\mu = 0.09$	$C_\mu = 0.09$	-
Sreenivasan (1998)	-	$(2/3)^{3/2} \times 0.424 = 0.231$	-
Loth (2001)	0.27	$1.6C_\mu^{3/4} = 0.263$	-
Yeung et al. (2001, 2006, $38 \leq R_\lambda \leq 648$)	-	-	0.78
Sommerfeld et al. (2008, section 4.3.3)	0.24	$(2/3)^{1/2} \times 0.3 = 0.245$	-
Ishihara et al. (2009)	-	$(2/3)^{3/2} \times 0.43 = 0.234$	-
Sawford and Yeung (2011, $38 \leq R_\lambda \leq 1000$)	-	-	0.74
Vassilicos (2015)	-	$0.218 \ldots 0.544$	-

3.3.2 Drag modification

The high turbulence intensity of flow in stirred-tanks has an appreciable effect on the mean drag force acting on the suspended particles. The recent review of Balachandar and Eaton (2010) shows that different mechanisms may be active and different phenomena are observed depending on the precise conditions, but a comprehensive understanding has not been achieved yet. For mechanically agitated dilute suspensions of particles, experimental work summarized by Fajner et al. (2008) shows that the settling velocity is typically smaller than that in a still fluid, which indicates an increase in the apparent drag force due to turbulence. The problem involves several relevant parameters (Good et al., 2014), most prominently the Stokes number St, i.e. the ratio of particle and turbulence timescales.

A quantitative model for the modification factor of the drag force due to turbulence was developed by Lane et al. (2005). Denoting the terminal velocity u_{term} in still fluid by an index "0" and that in turbulent flow by an index "T", their correlation is expressed as[‡]:

$$\frac{u_{\mathrm{term,T}}}{u_{\mathrm{term,0}}} = 1 - 1.18St^{0.7}\exp(-0.47St). \tag{17}$$

[‡] Note that a different definition of the turbulence integral timescale is used here (see section 3.3.1), hence the resulting constants in Eq. (17) are different from those given in Lane et al. (2005).

This translates to

$$\frac{C_{\mathrm{D,T}}}{C_{\mathrm{D},0}} = \left(\frac{u_{\mathrm{term,T}}}{u_{\mathrm{term},0}}\right)^{-2} \tag{18}$$

for a corresponding modification factor of the drag coefficient. The Stokes number St gives the ratio of the particle relaxation time in a stagnant fluid $\tau_S = 4d_\mathrm{p}(\rho_S/\rho_L + C_\mathrm{VM})/\left(3C_{\mathrm{D},0}u_{\mathrm{term},0}\right)$ to the turbulence timescale. For the latter, Lane et al. (2005) simply took the Lagrangian integral timescale following the fluid motion T_L^L.

The correlation of Lane et al. (2005), Eq. (17), is based on a summary of data from both experiment and simulation available at that time. Since all of these data were taken at rather low values $St < 1$, a form of the functional dependence was imposed, which ensured that the still-fluid values are approached for both the limits of low and high Stokes numbers in accordance with the general expectation (Good et al., 2014). It is noteworthy that data for both solid particles and gas bubbles are represented in a unified manner by Eq. (17). This can be understood by a mechanism proposed by Spelt and Biesheuvel (1997), which is based on the lift force acting on the particle or bubble. Assuming small enough particle / bubble size such that the lift coefficient is positive (which is the case for all available data and also for the present applications), they argued for bubbles that the lift force acts to move them preferentially to regions where the turbulent fluctuation velocity is directed downwards. On average this leads to a lower rise velocity, which can be modeled by an increased drag coefficient. Particles will in contrast be moved preferentially to regions where the turbulent fluctuation velocity is directed upwards. But this leads again to a lower settling velocity and hence can also be modeled by an increased drag coefficient.

The fact that the Lagrangian integral timescale following the fluid motion T_L^L was used to define the Stokes number, rather than particle-turbulence interaction timescale T_L^S has led us to re-evaluate the model of Lane et al. (2005), Eq. (17). Considering that the drag modification results from an interaction between particles and turbulence, use of the latter seems more appropriate. Moreover, T_L^S takes into account the crossing trajectories effect. Due to the appearance of the ratio $k^{1/2}/u_\mathrm{rel}$ (see Eq. (13a, b)), this at least in principle captures also the dependence of the drag modification on this second parameter, which is well-known from experimental and simulation studies (Spelt and Biesheuvel, 1997; Poorte and Biesheuvel, 2002). A more recent experimental investigation by Doroodchi et al. (2008) showed that when the particle size becomes comparable to the turbulent lengthscale, the parameter d_p/Λ has an effect, too. If this parameter is small, the drag modification is expected to become independent thereof. Our re-evaluation includes the data from Doroodchi et al. (2008) as well as simulation data from Mazzitelli et al. (2003) in addition to the data from Spelt and Biesheuvel (1997), Brucato et al. (1998b), and Poorte and Biesheuvel (2002), on which the original proposal of Lane et al. (2005) was based. The results are shown in Figure 1.

Figure 1 (a) employs the original definition of the Stokes number based on T_L^L as in Lane et al. (2005). The doubly logarithmic scaling makes the deviations between the correlation and the data more readily apparent, but also the deviations between different datasets. The additional data from Mazzitelli et al. (2003) blend quite well with the originally used ones, while the data from Doroodchi et al. (2008) are rather distinct and poorly represented by the correlation Eq. (17) with this definition of the Stokes number.

In Figure 1 (b) the presently proposed definition of the Stokes number in terms of T_{L}^{S} is used. At lower values of $St < 1$ most of the data now show a somewhat more coherent trend. There is one exceptional dataset from Spelt and Biesheuvel (1997, red squares with crosses), which now exhibits a distinct behavior. This dataset differs from all others by a rather high value of the parameter d_{p}/Λ as shown in the legend. As discussed above, under this circumstance a different behavior could be expected. The data from Doroodchi et al. (2008) now appear at significantly higher values of the Stokes number and much more in line with the trend suggested by the functional form of Eq. (17) (but now with a different definition of St). Since these data are also taken at rather high values of d_{p}/Λ, however, this agreement may just be fortunate. A last noteworthy observation is that another one of the datasets from Spelt and Biesheuvel (1997, green empty squares), which appeared at a single value of St in Figure 1 (a) now is spread over a range of values.

Comparing Figure 1 (a) and (b), it may be stated that at least the same quality of agreement is possible by basing the definition of the Stokes number on T_{L}^{S} rather than on T_{L}^{L}. This takes into account the crossing trajectories effect and provides a possibility to include the dependence on a second relevant parameter, namely $k^{1/2}/u_{\mathrm{rel}}$, in addition to $\tau_S/T_{\mathrm{L}}^{L}$. Moreover this definition is commonly used in models of turbulent dispersion (e.g. de Bertodano (1998), see section 3.3.3) so that a unified description of both aspects is obtained. Some reservation has to be made, that cases with $d_{\mathrm{p}}/\Lambda > 0.1$ may require a more elaborated model accounting for the dependency of the drag modification also on this third parameter.

For a quantitative model, we keep the functional form suggested by Lane et al. (2005) and fit the parameter values to the data of Figure 1 (b). Data with $d_{\mathrm{p}}/\Lambda > 0.1$, for which this form may not be adequate (symbols colored in red), have been excluded from the fit. The re-evaluated correlation becomes

$$\frac{u_{\mathrm{term,T}}}{u_{\mathrm{term,0}}} = 1 - 2.23St^{1.4}\exp(-St), \tag{19}$$

where the Stokes number is defined as $St = \tau_S/T_{\mathrm{L}}^{S}$. It is shown as the solid line in Figure 1 (b). The steep decrease of the drag modification factor in the range $0.1 < St \leq 1$ is captured much better by the revised correlation Eq. (19) than by just changing the definition of St in Eq. (17), which is shown as the dashed line in Figure 1 (b). Upon further increasing St both correlations reach a minimum at $St \approx 1.5$, where unfortunately insufficient data are available to precisely judge the lowest occurring value. Beyond $St \approx 10$ both correlations approach unity. The agreement with the data of Doroodchi et al. (2008) at higher St is surprising as these were not included in fitting the correlations.

Based on these findings, the presently proposed correlation, Eq. (19), is applied to model the effect of turbulence on the drag force as it represents the best currently available description, although there remains an obvious need for further research to fill the mentioned gaps in understanding.

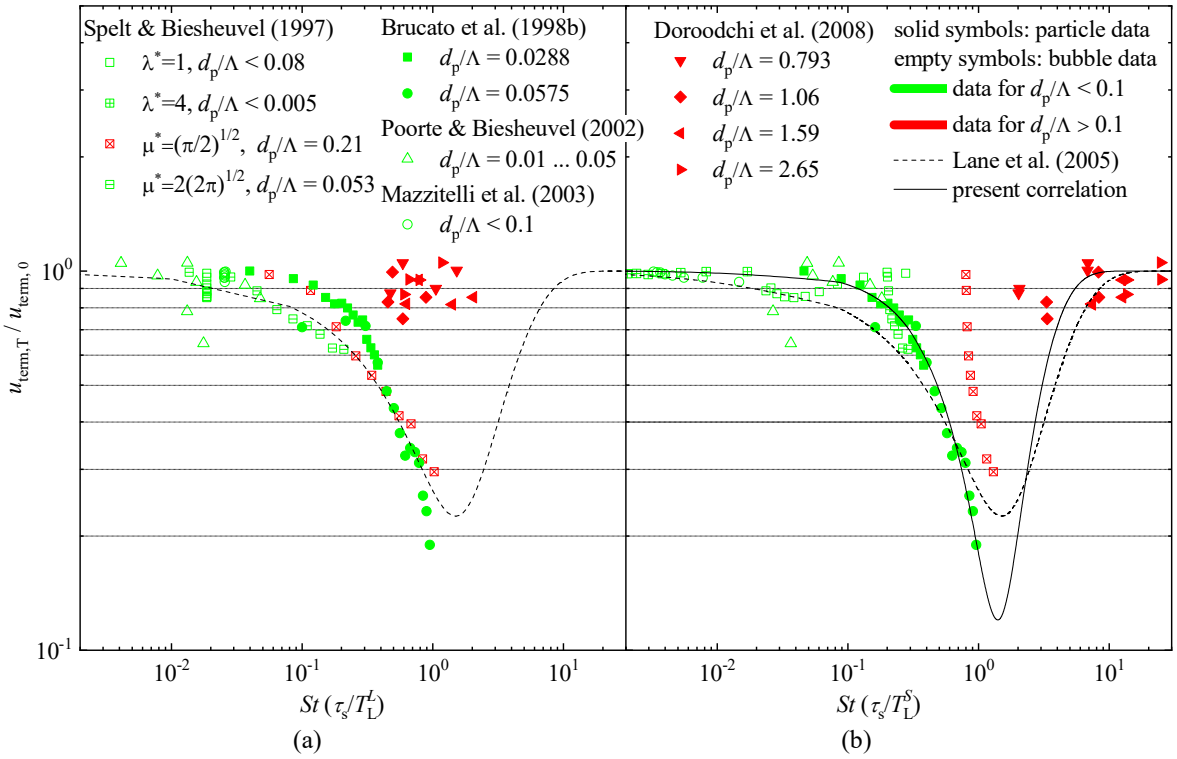

Figure 1. Predictions for the drag modification factor $u_{\mathrm{term,T}}/u_{\mathrm{term,0}}$ according to the presently proposed correlation, Eq. (19), and the earlier one from Lane et al. (2005), Eq. (17), (represented by solid and dashed lines, respectively) for $10^{-3} < St \leq 30$ compared with experimental and simulation data. Solid and empty symbols denote particle and bubble data, respectively. Green and red colors denote data for $d_\mathrm{p}/\Lambda < 0.1$ and $d_\mathrm{p}/\Lambda > 0.1$, respectively. The Stokes number is defined as $St = \tau_S/T_\mathrm{L}^L$, i.e. as in Lane et al. (2005), in part (a) and as $St = \tau_S/T_\mathrm{L}^S$, i.e. as proposed here, in part (b).

3.3.3 Turbulent dispersion

Turbulent dispersion is significant when the size of the turbulent eddies is larger than the particle size. In stirred tank flows, as indicated in section 2.3, the particle size ($0.1\ \mathrm{mm} \leq d_\mathrm{p} \leq 1\ \mathrm{mm}$) is larger than the Kolmogorov lengthscale ($O(10^{-2})$ mm) but at least an order of magnitude smaller than that of the energy-containing eddies ($O(10^{1})$ mm). As a result, turbulent dispersion will be significant.

A rational way to study turbulent dispersion in turbulence is the probability density function (PDF) approach, which is based on a phase-space formulation of the particle equation of motion including turbulent fluctuations. A comprehensive review of different dispersion models obtained using this approach can be found in Reeks, Simonin, and Fede (2017). For simulations concerning solid dispersion in stirred tank flows, a frequently used model is the one proposed by Reeks (1991). Following de Bertodano (1998) the resulting turbulent dispersion force takes the form[§]

[§] The original version of this correlation (Reeks, 1991) is derived based on the assumption of low Re_p (so that the Stokes drag obeys), while later de Bertodano (1998) found it applicable to describe turbulent dispersion also for conditions with moderate Re_p.

$$\boldsymbol{F}_S^{\mathrm{disp}} = -C_{\mathrm{D},0}\frac{1}{2}d_{\mathrm{p}}^{-1}\rho_L u_{\mathrm{rel}}\frac{1}{1+St}T_{\mathrm{L}}^{S}k\nabla\alpha_S. \tag{20}$$

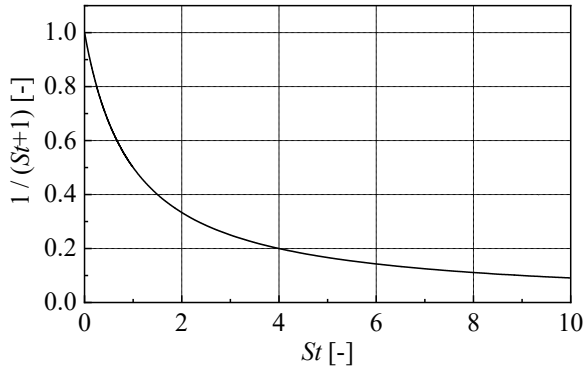

Figure 2. Variation of the magnitude of the turbulent dispersion force.

For later reference, the variation of the magnitude of the turbulent dispersion force with increasing Stokes number is illustrated in Figure 2.

An alternative approach is to apply Reynolds-decomposition and -averaging also to the modeled drag force. The most frequently used model following this approach is the Favre averaged drag (FAD) model proposed by Burns et al. (2004), where a similar form as Eq. (20) but with $St = 0$ is obtained. For non-inertial particles, i.e. in the limit $St \to 0$, the turbulent dispersion forces obtained by the PDF and FAD approaches agree. However, the effect of particle inertia is not accounted for by the FAD approach, which thus would predict too strong dispersion for inertial particles.

3.4 SSG Reynolds stress model

Only the turbulence in the continuous phase is considered, i.e. the dispersed phase model is applied. The index 'L' is then dropped throughout this section for notational convenience. The transport equation for the Reynolds stress tensor $\mathbf{R} = \langle \boldsymbol{u}' \otimes \boldsymbol{u}' \rangle$ is given as

$$\begin{aligned}\frac{\partial}{\partial t}(\alpha\rho\mathbf{R}) + \nabla\cdot(\alpha\rho\boldsymbol{u}\otimes\mathbf{R}) = {} & \nabla\cdot\left(\alpha\left(\boldsymbol{\mu}^{\mathrm{mol}} + C_s\boldsymbol{\mu}^{\mathrm{turb}}\right)\nabla\otimes\mathbf{R}\right) \\ & + \alpha\rho\left(\mathbf{P} + \boldsymbol{\phi} - \frac{2}{3}\varepsilon\mathbf{I} + \mathbf{G}\right),\end{aligned} \tag{21}$$

and that for the isotropic turbulent dissipation rate ε as

$$\begin{aligned}\frac{\partial}{\partial t}(\alpha\rho\varepsilon) + \nabla\cdot(\alpha\rho\boldsymbol{u}\varepsilon) = {} & \nabla\cdot\left(\alpha\left(\boldsymbol{\mu}^{\mathrm{mol}} + C_\varepsilon\boldsymbol{\mu}^{\mathrm{turb}}\right)\cdot\nabla\varepsilon\right) \\ & + \alpha\rho\frac{\varepsilon}{k}\left(C_{\varepsilon,1}\frac{1}{2}tr(\mathbf{P}) - C_{\epsilon,2}\varepsilon\right).\end{aligned} \tag{22}$$

Individual terms appearing on the right side of equation (21) describe diffusion, production, pressure-strain correlation, dissipation, and generation due to body forces (here frame rotation).

Compared with isotropic two-equation turbulence models (like for instance the $k-\omega$ SST model), the diffusion term here involves tensorial viscosities:

$$\boldsymbol{\mu}^{\mathrm{mol}} = \mu^{\mathrm{mol}}\mathbf{I}, \qquad \boldsymbol{\mu}^{\mathrm{turb}} = \frac{\rho k}{\varepsilon}\mathbf{R}, \tag{23}$$

the latter of which is anisotropic. The production term **P** is evaluated exactly in terms of the velocity gradient $\nabla \boldsymbol{u}$ and **R**, and its component notation reads

$$P_{ij} = -\left(\frac{\partial u_i}{\partial x_k}R_{jk} + \frac{\partial u_j}{\partial x_k}R_{ik}\right). \tag{24}$$

The generation term **G** due to frame rotation is given in component notation as

$$G_{ij} = 2\mu^{\mathrm{mol}}\Omega_k\left(D_{im}\varepsilon_{jkm} + D_{jm}\varepsilon_{ikm}\right), \tag{25}$$

where **D** is the strain rate tensor, $\boldsymbol{\Omega}$ the frame angular velocity, and ε_{ijk} is the Levi-Chivita factor defined by

$$\varepsilon_{ijk} = \begin{cases} 1, & \text{if } (i,j,k) \text{ are cyclic,} \\ -1, & \text{if } (i,j,k) \text{ are anticyclic,} \\ 0, & \text{otherwise.} \end{cases} \tag{26}$$

Since $tr(\mathbf{G}) = 0$ from the definition Eq. (25) it does not appear in the equation for the turbulent dissipation rate, Eq. (22).

Considerable attention has been devoted to the modeling of the pressure-strain correlation $\boldsymbol{\phi}$ due to its crucial role in redistributing the Reynolds stress components. According to Speziale, Sarkar, and Gatski (1991) this term is given in component notation as

$$\begin{aligned} \phi_{ij} = &-\left[C_{1a}\varepsilon + C_{1b}\frac{1}{2}tr(\mathbf{P})\right]A_{ij} + C_2\varepsilon\left[A_{ik}A_{kj} - \frac{1}{3}A_{mn}A_{mn}\delta_{ij}\right] \\ &+\left[C_{3a} - C_{3b}\left(A_{ij}A_{ij}\right)^{\frac{1}{2}}\right]kD_{ij} + C_4k\left[A_{ik}D_{jk} + A_{jk}D_{ik} - \frac{2}{3}A_{mn}D_{mn}\delta_{ij}\right] \\ &+C_5k\left(A_{ik}W_{jk} + A_{jk}W_{ik}\right), \end{aligned} \tag{27}$$

where **A** and **W** denote the anisotropy and rotation rate tensors, respectively, with components

$$A_{ij} = \frac{R_{ij}}{2k} - \frac{1}{3}\delta_{ij}, \quad W_{ij} = \frac{1}{2}\left(\frac{\partial u_i}{\partial x_j} - \frac{\partial u_j}{\partial x_i}\right) + \varepsilon_{ijk}\cdot\Omega_k\,. \tag{28}$$

For the coefficients appearing in the equations above, the standard values of ANSYS CFX (ANSYS 2018) have been used, which are summarized in Table 5.

Table 5: Coefficient values for the SSG RSM.

ε-equation	C_ε	$C_{\varepsilon 1}$	$C_{\varepsilon 2}$					
	0.18	1.45	1.83					
R-equations	C_s	C_{1a}	C_{1b}	C_2	C_{3a}	C_{3b}	C_4	C_5
	0.22	3.40	1.80	4.20	0.80	1.30	1.25	0.40

4 DESCRIPTION OF THE SIMULATIONS

4.1 Investigated tests

The data used for validation should contain information on the volume fraction and average velocities so that the modeling of the particle forces may be validated independently. Data relating to fluctuating velocities such as TKE or Reynolds stresses are needed in order to judge the quality of the turbulence model. According to the literature overview of section 2.2, the following datasets were selected to provide a comprehensive validation database that meets the criteria above: Nouri and Whitelaw (1992), Guha et al. (2007), Montante et al. (2012), and Tamburini et al. (2013). In addition, the LES simulation from Guha et al. (2008) is considered as well, since it provides highly resolved simulation results matching the experiment of Guha et al. (2007). For most experiments, a standard tank configuration (Shi and Rzehak, 2018) was used. The solid fraction considered was at most 1% in all experiments so as to satisfy a dilute suspension condition. All selected cases correspond to complete suspension conditions. Other experimental details are summarized in Table 6.

Nouri and Whitelaw (1992) conducted both single and two-phase flow studies in a 294 mm diameter tank with an impeller rotation speed of 313 rpm. Measurements were performed in a vertical plane placed mid-way between two baffles, and only solid phase information was provided in the two-phase flow measurement. Radial profiles of mean velocities in axial and tangential directions and fluctuation velocity in the axial direction were measured at three horizontal positions of z/H = 0.068, 0.510, and 0.782. In the near impeller region, axial profiles of mean velocities in radial and axial directions were measured at two axial positions of $2r/D_t$ = 0.347 and 0.463 in the range of $-1.5 \leq 2z_{bla}/H_{bla} \leq 1.5$ (with z_{bla} denoting the axial coordinate with the origin at the impeller disk). An axial profile of local solid fraction was measured at the radial position of $2r/D_t$ = 0.136.

Also both single and two-phase flow were investigated by Montante et al. (2012) with a 232 mm diameter tank and an impeller rotation speed of 852 rpm. Measurements were performed in a vertical plane in between z/H = 0.2 and z/H = 0.6 placed mid-way between two baffles. Axial profiles of radial and axial components of both mean and fluctuating liquid velocities were measured at $2r/D_t$ = 0.88 and 0.96.

A two-phase flow system was studied by Guha et al. (2007) with a 200 mm diameter tank and an impeller rotation speed of 1000 rpm. Measurements were conducted via the CARPT technique and only azimuthally averaged quantities were provided. Radial profiles of mean solid velocities in radial, axial, and tangential directions were measured at three horizontal positions of z/H = 0.075, 0.34, and 0.65. The corresponding LES simulation of Guha et al. (2008) additionally provides a radial profile of local solid fraction at a horizontal position of z/H = 0.34.

Another two-phase flow system was investigated by Tamburini et al. (2013) with a 190 mm diameter tank and impeller rotation speeds ranging from 300 to 600 rpm. Differing from the standard configuration, the tank here was un-baffled and the turbine diameter was half that of the tank diameter. Measurements were performed in a vertical plane placed mid-way between two baffles, where in contrast to the previous works radially averaged axial profiles of solid fraction are provided.

Table 6: Parameters for the investigated test cases.

Reference	D_t (mm)	C_i (mm)	H_{bla} (mm)	Ω (rpm)	u_{tip} (m s^{-1})	ρ_S/ρ_L (-)	$\bar{\alpha}_{S,ave}$ (%)	d_p (mm)	Available data
Nouri and Whitelaw (1992)	294	73.5	19.6	313	1.61	-	-	-	$\bar{u}_r, \bar{u}_z, \bar{u}_\theta; u'_z$
Montante et al. (2012)	232	77.3	15.5	852	3.45	-	-	-	$\bar{u}_r, \bar{u}_z; u'_r, u'_z$
Nouri and Whitelaw (1992)	294	73.5	19.6	313	1.61	1.32	0.50	0.665	$\bar{u}_{S,r}, \bar{u}_{S,z}, \bar{u}_{S,\theta}; \bar{\alpha}_S$
Guha et al. (2007, 2008)	200	66.7	13.3	1000	3.49	2.50	1.00	0.300	$\bar{u}_{S,r}, \bar{u}_{S,z}, \bar{u}_{S,\theta}; \bar{\alpha}_S$ (LES)
Montante et al. (2012)	232	77.3	15.5	852	3.45	2.47	0.05	0.115	$\bar{u}_{L,r}, \bar{u}_{L,z}; u'_{L,r}, u'_{L,z}$
							0.05	0.775	$\bar{u}_{L,r}, \bar{u}_{L,z}; u'_{L,r}, u'_{L,z}$
							0.15	0.775	$\bar{u}_{L,r}, \bar{u}_{L,z}; u'_{L,r}, u'_{L,z}$
Tamburini et al. (2013)	190	63.3	19.0	300	1.49	2.48	0.0081	0.138	$\bar{\alpha}_S$
				600	2.98	2.48	0.0081	0.138	$\bar{\alpha}_S$

4.2 Solution domain, boundary conditions and numerical approach

ANSYS CFX release 19.2 is used for the numerical simulations. This software solves the three-dimensional unsteady Reynolds-averaged Navier-Stokes equations with a control volume based finite-element discretization. For the problem considered, the advection terms are discretized using the high resolution scheme proposed in Barth and Jesperson (1989), while the solution is advanced in time with a second order backward Euler scheme. Other details regarding the discretization of the diffusion and pressure gradient terms as well as the solution strategy are detailed in ANSYS Inc. (2018, section 11).

The simplification of the computational domain, the arrangement concerning the position of the baffles and the impellers, and the implementation of the mixing-plane model of the MRF method (ANSYS Inc., 2018) to couple the results from the rotating and the static blocks can be found in Shi and Rzehak (2018). A still and homogeneous suspension is taken as the initial condition. On the walls no-slip and free slip conditions are applied for the liquid and solid phases, respectively, while the scalable wall function is used to specify the wall boundary condition in SSG RSM turbulence model. At the top of the suspension, a free slip wall is introduced.

Fully structured meshes are used for all investigated cases (see Table 7 for the mesh details) with comparable average spacings in radial, azimuthal, and axial direction as those of Shi and Rzehak (2018), where geometries of similar dimensions were investigated. To avoid numerical difficulties, for each case, the calculation is performed at first in pseudo-transient mode for 50 rotations and then switched to transient mode for 20 rotations. The time step for each stage is set again in accordance with Shi and Rzehak (2018) such that a rotation of 4° per time step results in order to achieve low residuals ($\leq 10^{-5}$). Averaged results are obtained during the last 10 rotations. Following these numerical settings, the adequacy of the resulting solutions was established in Shi and Rzehak (2018), in which test cases with impeller rotation speed up to 450 rpm were considered. Since a higher impeller rotation speed is involved in some of the investigated cases, a further grid independency study is presented in Appendix A, where results for the mean and fluctuation velocities are discussed for the single-phase flow case of Guha et al. (2007) with an impeller rotation speed of 1000 rpm.

Table 7: Parameters for meshes for all investigated test cases.

Test case	Tank volume			Impeller blade			Overall	CPU time (with 32 processors)
	N_r	N_θ	N_z	N_r	N_θ	N_z	N_{tot}	
Nouri and Whitelaw (1992)	120	150	150	36	5	36	2.70×10^6	276 h
Guha et al. (2007)	101	120	120	30	4	30	1.45×10^6	130 h
Montante et al. (2012)	95	120	131	22	4	32	1.49×10^6	144 h
Tamburini et al. (2013)	115	99	108	36	3	36	1.23×10^6	100 h

For unsteady RANS simulations conducted in multiple reference frames, the calculation of averages and fluctuations needs to be carefully considered in order to match the experimentally obtained values. For a detailed discussion, the reader is referred once again to Shi and Rzehak (2018).

5 RESULTS AND DISCUSSION

5.1 Single-phase results

Single-phase flow simulations are conducted first to get an idea of the performance that can be expected for a RANS turbulence model, namely the SSG RSM. Model assessment is done first for the mean liquid velocity and then for the liquid velocity fluctuations using the data of Nouri and Whitelaw (1992) and Montante et al. (2012). For both, mean and fluctuations, this comprises several profiles along radial and axial directions throughout the entire free flow region in the tank between the impeller and the baffles and all three components of velocity.

5.1.1 Mean velocity

Figure 3 compares simulation results for radial profiles of tangential and axial mean liquid velocity with the measured data from Nouri and Whitelaw (1992). At all three heights of $z/H = 0.068$, 0.510, and 0.782, generally very good agreement with the experimental data is achieved by the current simulation. Along the radial direction, some deviation from the measured data can be observed at $0.05 \leq 2r/D_t \leq 0.15$ (i.e. the region near the tank shaft) and $0.9 \leq 2r/D_t \leq 1$ (i.e. the region near the tank wall).

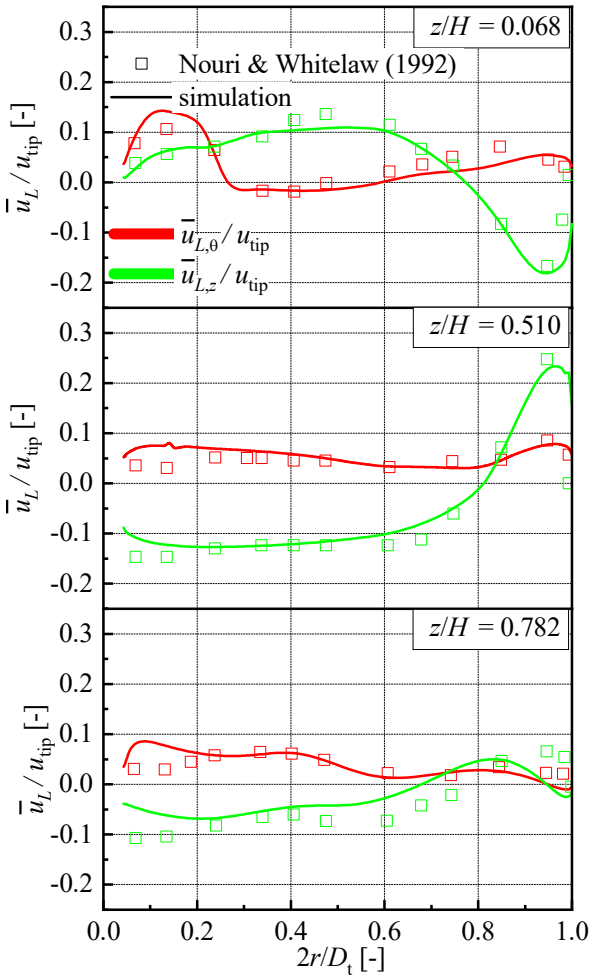

Figure 3. Comparison of present simulation results (lines) and measured data (symbols) from Nouri and Whitelaw (1992) for the tangential (red) and axial (green) components of mean liquid velocity. Radial profiles over the entire tank radius are shown at different heights as indicated on each panel.

Comparisons of axial profiles of mean fluid velocity between the simulations and the measured data from Nouri and Whitelaw (1992) and Montante et al. (2012) are shown in Figure 4 and Figure 5, respectively. Only data for the radial component of mean liquid velocity are provided by Nouri and Whitelaw (1992). Also, as shown in Figure 4, only a portion of the tank height around the impeller has been considered. The predicted peak values at both radial positions are in quantitative agreement with the ones observed in the experiment, but the predicted profiles show a bit narrower structures than found in the measured data.

The experiment of Montante et al. (2012) provides data for radial and axial components of mean liquid velocity at the radial position of $2r/D_t = 0.88$, which is close to the tank wall. The predicted axial component agrees quite well with the measured data, however the peak of the radial component is significantly overestimated.

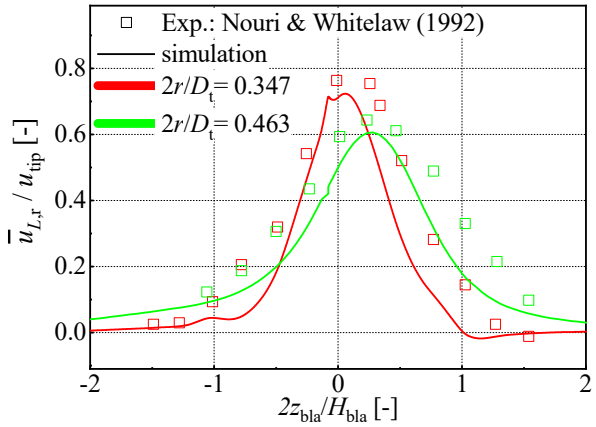

Figure 4. Comparison of present simulation results (lines) and measured data (symbols) from Nouri and Whitelaw (1992) for the radial component of mean liquid velocity in the near impeller region at $2r/D_t = 0.347$ (red) and $2r/D_t = 0.463$ (green). Axial profiles restricted to a height range around the impeller are shown.

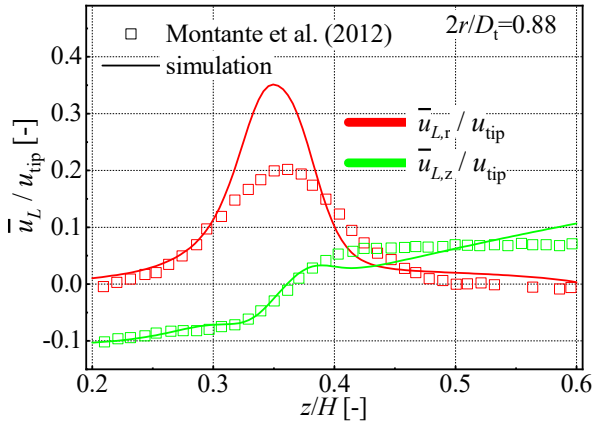

Figure 5. Comparison of present simulation results (lines) and measured data (symbols) from Montante et al. (2012) for the radial (red) and axial (green) components of mean liquid velocity. Axial profiles restricted to a height range of $0.2 \leq z/H \leq 0.6$ are shown at a radial position of $2r/D_t = 0.88$.

In summary, taken together with the single-phase results from Shi and Rzehak (2018), it may be stated that for the mean velocities good predictions are obtained at lower rotation speeds Ω at least up to 450 rpm, while deviations occur at higher values certainly from 850 rpm on. Where deviations occur, the most prominent ones are localized near the impeller blades and less significant ones near the tank wall and impeller shaft.

5.1.2 Turbulent fluctuations

Radial profiles for the fluctuating liquid velocity are provided by Nouri and Whitelaw (1992) at heights of $z/H = 0.068$ and 0.51. For the former, both tangential and axial components are available, while for the latter only the axial component is provided. As seen in Figure 6, the agreement between simulation and experiment is good for the component at the higher measurement position. At the lower measurement position, which is quite close to the tank bottom, a moderate underprediction is seen for the axial component and a larger one for the tangential component. The proximity of the tank bottom suggests that this is deviation might be caused by a wall-effect, which is a known issue in standard RSMs (Launder and Sandham, 2002, section 2).

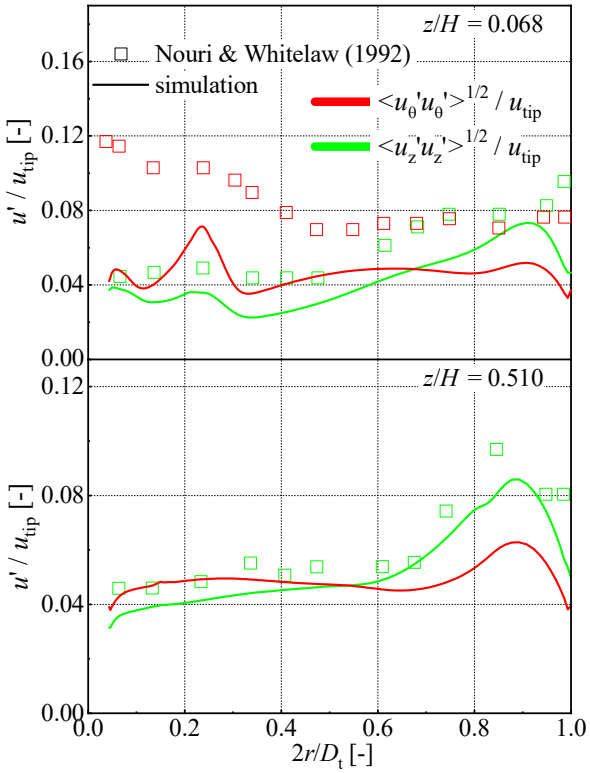

Figure 6. Comparison of present simulation results (lines) and measured data (symbols) from Nouri and Whitelaw (1992) for the tangential (red) and axial (green) components of fluctuating liquid velocity. Radial profiles over the entire tank radius are shown at different heights as indicated on each panel.

Figure 7 compares predictions of the axial profiles of the radial and axial components of fluctuating liquid velocity at the radial positions of $2r/D_t$ = 0.88 and 0.96 with the measured data from Montante et al. (2012). According to the measured data, the radial component is larger than the axial one in the impeller stream (i.e. for roughly $0.25 < z/H < 0.45$) and becomes smaller than the latter at regions outside the impeller stream. This qualitative feature is captured by the predictions while the quantitative agreement is only mediocre. Farther away from the tank wall, at $2r/D_t$ = 0.88, both fluctuation components are significantly underestimated. Nearer to the wall, at $2r/D_t$ = 0.96, deviations are much less severe with both over- and underestimation occurring in different parts of the profiles.

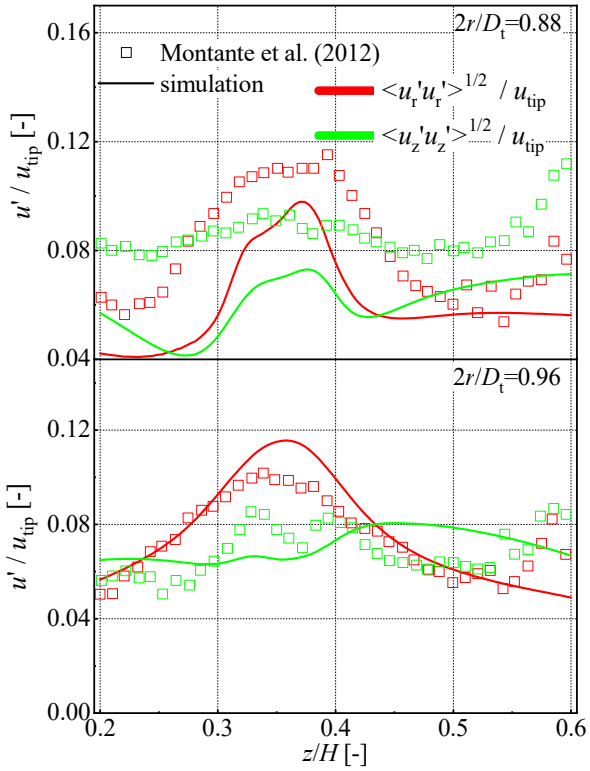

Figure 7. Comparison of present simulation results (lines) and measured data (symbols) from Montante et al. (2012) for the radial (red) and axial (green) components of fluctuating liquid velocity. Axial profiles restricted to a height range of $0.2 \leq z/H \leq 0.6$ are shown are shown at different radial positions as indicated on each panel.

In summary, again taken together with the single-phase results from Shi and Rzehak (2018), it may be stated that for the turbulent fluctuations, reasonable predictions are only obtained at very low rotation speeds Ω smaller than 200 rpm. At larger values of Ω mostly only mediocre agreement with the measured values is found though qualitative features of the data are reproduced.

5.2 Two phase results

The full model presented in section 3 will be taken as a baseline for the investigation of two-phase flows. In addition, seven reduced model variants, summarized in Table 8, are considered to highlight the importance of various aspects. Two model variants termed T-0.1 and T-0.5 use identical particle forces as the baseline model, but adopt different settings of the integral timescale T_{L}^{L}, namely $0.1\,k/\varepsilon$ and $0.5\,k/\varepsilon$ as opposed to $0.224\,k/\varepsilon$ for the baseline model. This choice potentially affects the turbulent dispersion force as well as the drag modification due to turbulence. The two model variants, drag-SN and drag-Lane, differ from the baseline model in the drag correlation. Compared with the baseline model, the former disregards the turbulence effects on the drag while the latter accounts for these effects by the model from Lane et al. (2005) which neglects the crossing trajectory effects. The model variant disp-FAD differs from the baseline model in the turbulent dispersion force correlation. Compared with the baseline model, turbulent dispersion is accounted for by the FAD model from Burns et al. (2004) which assumes negligible particle inertia and approaches the baseline model in the limit $St \rightarrow 0$. Effects of the lift and virtual mass forces are assessed by the model variants lift-off and vm-off, respectively, where one of the forces is simply turned off from the baseline model.

Validation of the baseline model is conducted taking the following approach. The selected two phase flow cases of Nouri and Whitelaw (1992) and Guha et al. (2007, 2008) provide relatively comprehensive data, which comprise experimental or LES data of both mean solid velocity and solid fraction for model validation and are considered first. Simulations applying the baseline model as well as all model variants listed in Table 8 are conducted for the two cases to confirm the advantage of the baseline model over all other model variants. Extension of the validation of the baseline model is then made by comparing the simulation results of the baseline model with the measured data from Montante et al. (2012) and Tamburini et al. (2013). The former experiment provides data for the mean and fluctuating liquid velocities and considers varying particle size and solids loading. The latter provides data for the axial profiles of the solid fraction and considers varying impeller rotation speed.

Table 8: Summary of particle force correlations used in the various models applied in the present work.

Model abbreviation	**Force correlations**			
	Drag	Turb. disp.	Lift	Virt. mass
baseline	Eqs. (18) & (19)	de Bertodano (1998, $T_{\mathrm{L}}^{L} = 0.224\,k/\varepsilon$)	Shi & Rzehak (2019)	$C_{\mathrm{VM}} = 0.5$
T-0.1	Eqs. (18) & (19)	de Bertodano (1998, $T_{\mathrm{L}}^{L} = 0.1\,k/\varepsilon$)	Shi & Rzehak (2019)	$C_{\mathrm{VM}} = 0.5$
T-0.5	Eqs. (18) & (19)	de Bertodano (1998, $T_{\mathrm{L}}^{L} = 0.5\,k/\varepsilon$)	Shi & Rzehak (2019)	$C_{\mathrm{VM}} = 0.5$
drag-SN	Schiller & Naumann (1933)	de Bertodano (1998, $T_{\mathrm{L}}^{L} = 0.224\,k/\varepsilon$)	Shi & Rzehak (2019)	$C_{\mathrm{VM}} = 0.5$
drag-Lane	Lane et al. (2005)	de Bertodano (1998, $T_{\mathrm{L}}^{L} = 0.224\,k/\varepsilon$)	Shi & Rzehak (2019)	$C_{\mathrm{VM}} = 0.5$
disp-FAD	Eqs. (18) & (19)	Burns et al. (2004)	Shi & Rzehak (2019)	$C_{\mathrm{VM}} = 0.5$
lift-off	Eqs. (18) & (19)	de Bertodano (1998, $T_{\mathrm{L}}^{L} = 0.224\,k/\varepsilon$)	-	$C_{\mathrm{VM}} = 0.5$
vm-off	Eqs. (18) & (19)	de Bertodano (1998, $T_{\mathrm{L}}^{L} = 0.224\,k/\varepsilon$)	Shi & Rzehak (2019)	-

The Stokes number $St = \tau_S/T_{\mathrm{L}}^{S}$ is an important parameter, which crucially affects the intensity of the drag and turbulent dispersion forces and, consequently, influences the resulting flow field. Therefore it is of interest to estimate the range of values that has to be expected. In the absence of theoretical estimates that are applicable to stirred tank flows, values from simulations using the baseline model are used for this purpose. For the case of Nouri and Whitelaw (1992) the calculated range of values is about $0.1 \leq St \leq 10$ as shown in Figure 8. The magnitude of St is relatively low in the bulk region, typically lower than 0.5, but increases dramatically near any no-slip wall. This increase is not surprising since when approaching the wall the turbulent kinetic energy k vanishes while the dissipation rate ε approaches its maximum (e.g. Wilcox, 2006). This results in vanishing values of T_{L}^{L} and, consequently, T_{L}^{S}. Moderate values of St within roughly $0.5 \leq St \leq 5$ appear along the impeller stream possibly due to the relatively higher values of dissipation rate appearing in this region (Sbrizzai et al., 2006). In the other three cases, the distribution of St obtained (not shown) does not differ too much from that in Nouri and Whitelaw (1992) although particles with smaller relaxation time are considered. This is likely due to the higher impeller rotation speed involved which causes a more turbulent flow with a smaller value of T_{L}^{L}.

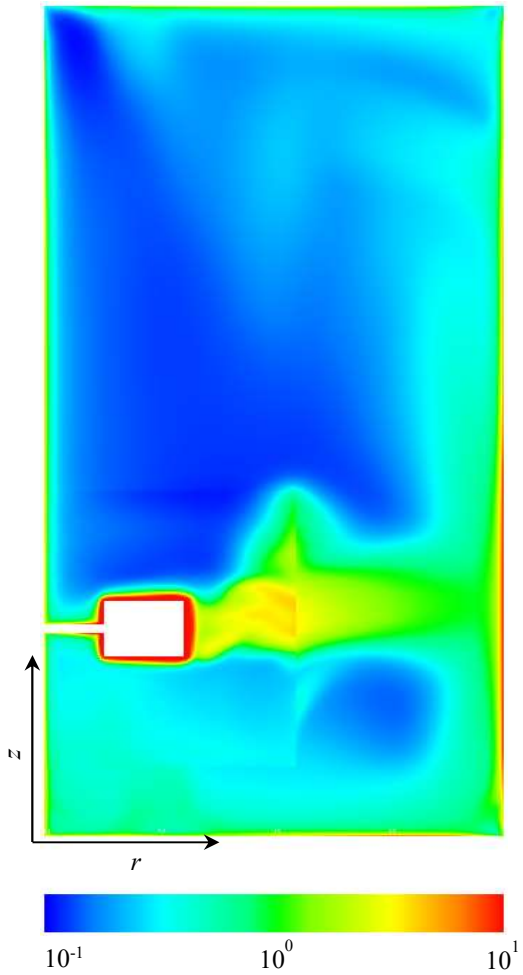

Figure 8. St calculated from the baseline model in the plane midway between two baffles for the case of Nouri and Whitelaw (1992). Results for $r \leq 0.57$ and $0.1 \leq h \leq 0.4$ are obtained by averaging the transient results in a frame rotating with the impeller while for the rest domain time averaged results are obtained in a laboratory frame.

5.2.1 Tests from Nouri and Whitelaw (1992)

Figure 9 (a) compares the predictions according to the model variants adopting different settings of the integral timescale T_{L}^{L} to the experimental data from Nouri and Whitelaw (1992) for the axial profile of the solid fraction at the radial position of $2r/D_{\mathrm{t}} = 0.136$. The effect of different settings is pronounced in the region below the impeller disk, namely for $z/H \leq 0.25$. Simulation results from the model variants T-0.1 and T-0.5 suffer, respectively, under- and overestimation compared to the experimental data, while good agreement is obtained by the baseline model. According to Figure 8 the typical Stokes number range in this region is from 0.5 to 1, within which the drag force is quite sensitive to the change in St (see Figure 1).

A similar comparison concerning the model variants adopting different drag correlations is shown in Figure 9 (b). When turbulence effects are taken into account the predicted profile shows a peak below the impeller disk, which is more pronounced with the variant drag-Lane than with the baseline model. For the model variant drag-SN, which neglects turbulence effects, this peak is absent. In quantitative terms, the baseline model comes much closer to the experimental data than

765 the variant drag-Lane. The variant drag-SN here performs also very good, but for a more precise
766 judgement experimental data in the vicinity of the impeller disk are unfortunately lacking. Above
767 the impeller disk only a slight difference between different model variants can be observed. Note
768 that the Stokes number in this region according to Figure 8 is around 10^{-1}, based on which the drag
769 modifications according to Lane et al. (2005) and to the present proposal are both very small.

770 Effects of different models concerning the non-drag forces are illustrated in Figure 9 (c). Compared
771 with the baseline prediction, the variant disp-FAD gives much lower solid fraction especially above
772 the impeller. Since the profile is taken quite close to the impeller shaft, where the Stokes number
773 ranges between 1 and 10 such a significant effect on the turbulent dispersion force may be expected
774 (see Figure 2). Neglecting the lift force on the other hand does not cause any big changes.

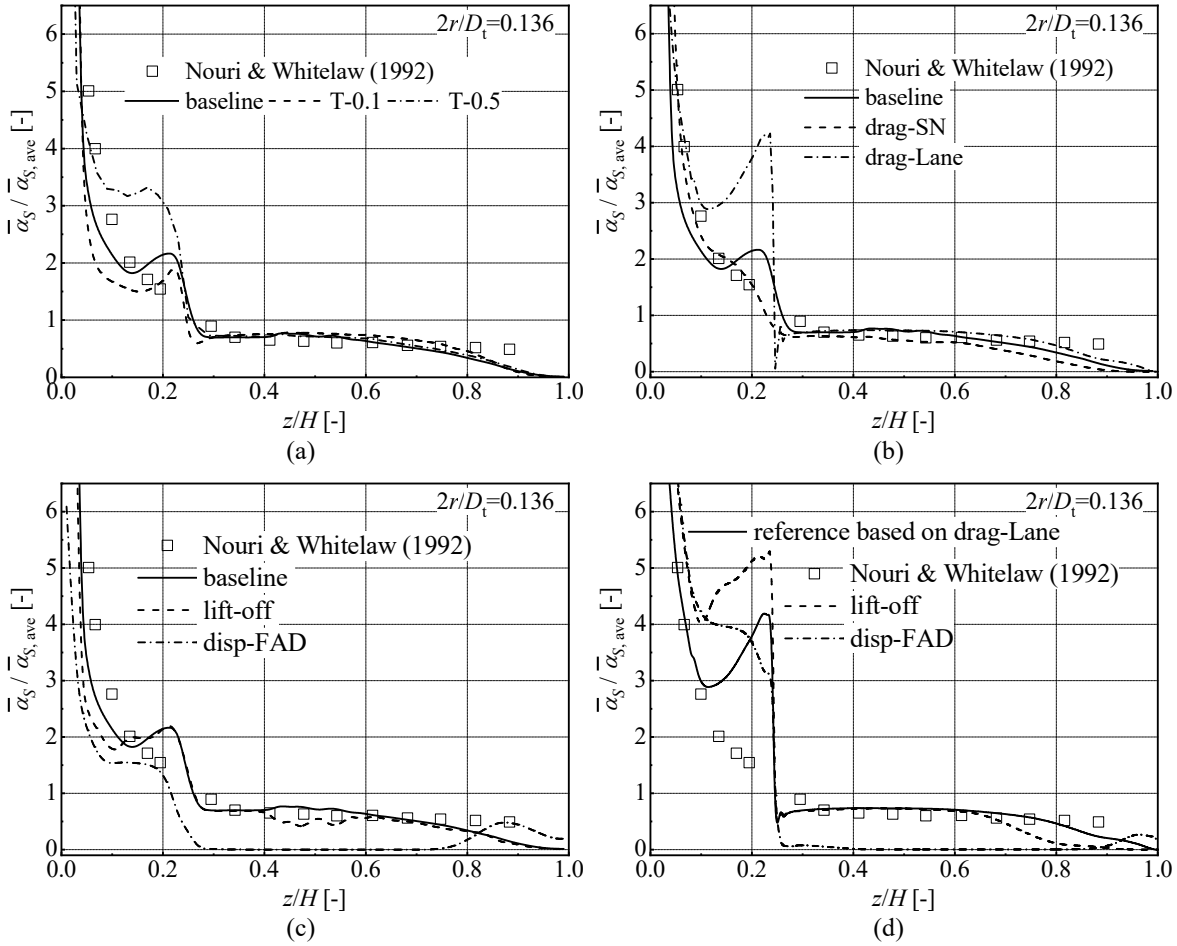

775
776
777
778

779 Figure 9. Comparison of the simulation results (lines) according to the baseline model and different model variants
780 indicated in Table 8 and measured data (symbols) from Nouri and Whitelaw (1992) for the solid fraction at $2r/D_t =$
781 0.136. Axial profiles over the entire tank height are shown.

782 However, these features are highly interdependent with other parts of the model. As seen in Figure
783 9 (d), when taking the variant drag-Lane as the reference model, both switching the turbulent
784 dispersion model from the one proposed by de Bertodano (1998) to the FAD model or turning off
785 the lift force results in a significant increase in the predicted solid fraction below the impeller disk,
786 i.e. for $z/H \leq 0.2$. These features are not surprising, as closures for the lift and turbulent dispersion

forces used in our simulation depend on the particle-fluid relative velocity, which is essentially affected by the drag law.

The predicted profiles of the model variant vm-off with either the baseline or the drag-Lane model taken as a reference (not shown in Figure 9 (c) and (d)) reveal hardly any difference from those using the reference models, which indicates a negligible effect of the virtual mass force here.

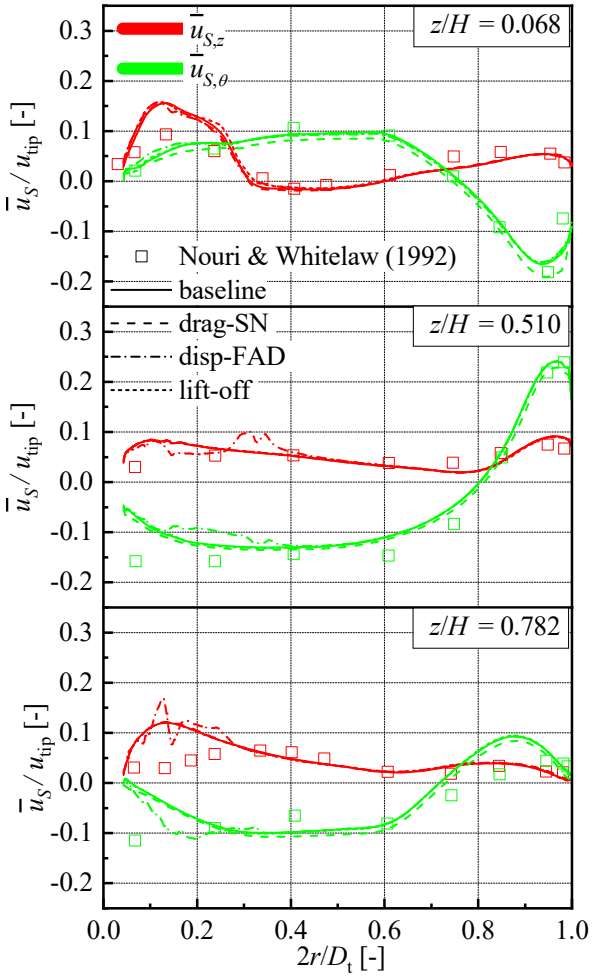

Figure 10. Comparison of the simulation results (lines) according to the baseline model and different model variants listed in Table 8 and measured data (symbols) from Nouri and Whitelaw (1992) for the axial (red) and tangential (green) components of mean solid velocity. Radial profiles over the entire tank radius are shown at different heights as indicated on each panel.

Figure 10 compares the model predictions to the measured data for the tangential and axial mean solid velocities along radial profiles at three different heights. Predictions according to some of the model variants, namely T-0.1, T-0.5, drag-Lane, and vm-off, are omitted as they show hardly any difference to that of the baseline model (represented by solid lines in Figure 10). Switching to the variant disp-FAD (represented by dash-dotted lines in Figure 10) introduces some erratic deviations in both components of the velocity in the lower half of the tank at the two heights above the impeller. To make absolutely sure that this observation is not caused by numerical effects, this case has been re-calculated by decreasing the time step in the transient mode from 4° to 1° per time step

and simultaneously increasing the number of rotations used for averaging from 10 to 20 rotations with no difference in the results. For the variant drag-SN (represented by dashed lines in Figure 10) a slight decrease in velocity is seen throughout. Turning off the lift force in variant lift-off (represented by short-dashed lines in Figure 10) has hardly any effect. Since concerning the solid faction, the effect of the lift force was much stronger when changing the reference to drag-Lane, this case was considered as well (not shown in the figure). It turns out that this change of reference model does not affect the results concerning the solid velocity.

Compared to the experimental data good agreement is found for the baseline predictions in the bulk region. In the region near the tank shaft, namely for $0.05 \leq 2r/D_\mathrm{t} \leq 0.15$, some deviation from the experimental data can be observed. This type of deviation appeared also in the single-phase tests and hence can be considered as a drawback of the RANS turbulence model.

A similar comparison concerning the radial component of the mean solid velocity at two radial positions near the impeller is given in Figure 11. The agreement of the baseline prediction with the experimental data is quite good. All model variants give almost identical profiles as the baseline model. As before only a selection of variants is shown in the figure, but the omitted ones have even smaller difference from the baseline model. The erratic deviation suffered by the variant disp-FAD in the bulk region does not occur here.

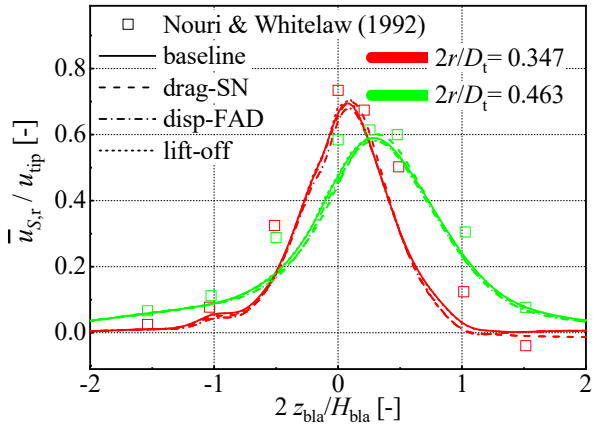

Figure 11. Comparison of the simulation results (lines) according to the baseline model and different model variants listed in Table 8 and measured data (symbols) from Nouri and Whitelaw (1992) for the radial component of mean solid velocity in the near impeller region. Axial profiles restricted to a height range around the impeller are shown at radial positions of $2r/D_\mathrm{t} = 0.347$ (red) and $2r/D_\mathrm{t} = 0.463$ (green).

5.2.2 Tests from Guha et al. (2007, 2008)

The comparison between the present predictions and the E-L / LES results from Guha et al. (2008) for the azimuthally averaged radial profile of the solid fraction at the height $z/H = 0.34$ is shown in Figure 12. A prominent feature of the E-L / LES results is the sharp peak near the wall. The presence of this peak is possibly a result of particle-wall collisions. Since these are not included in the baseline model, it is not surprising that such a near-wall peak does not appear in all the current predictions. Except for the near wall region the agreement of the baseline prediction with the E-L / LES results is generally acceptable. Results according to the variants T-0.1 and T-0.5 shown in Figure 12 (a) give, respectively, higher and lower values of solid fraction for $2r/D_\mathrm{t} \geq 0.4$. Approaching $2r/D_\mathrm{t} = 0.3$ both predict slightly higher solid fraction. In the region $0.3 \leq 2r/D_\mathrm{t} \leq 0.4$ the azimuthally averaged Stokes number (not shown in Figure 8) at the height of the impeller

disk has a typical value of $St \approx 1$, which is close to the critical value where according to Figure 1 (b) the strongest drag modification occurs. Departure from this critical value by either an increase or a decrease in St results in weaker drag modification.

Figure 12 (b) illustrates the effects of individual interfacial forces. The variant drag-SN predicts a significantly higher value of solid fraction compared with the baseline prediction in the region $0.3 \leq 2r/D_t \leq 0.4$ and deviates strongly from the E-L / LES results. The prediction according to the variant disp-FAD shows good agreement with the baseline prediction, which is different from the findings concerning the axial profile of solid fraction in the case of Nouri and Whitelaw (1992). Predictions according to all other variants, namely drag-Lane (not shown), lift-off, and vm-off (not shown) show hardly any difference compared with the baseline prediction.

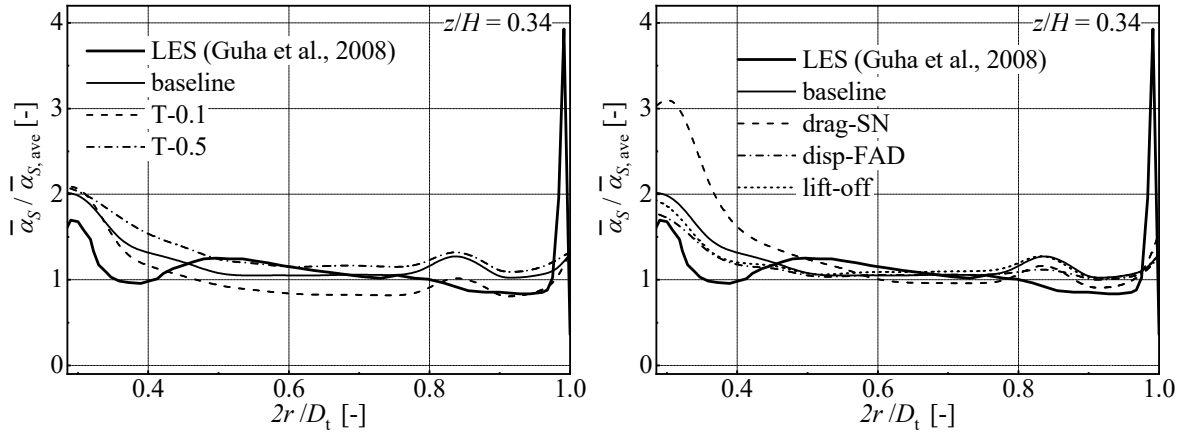

Figure 12. Comparison of the simulation results (lines) according to the baseline model and different model variants listed in Table 8 and the LES result (thick solid lines) from Guha et al. (2008) for azimuthally averaged radial profile of solid fraction at the height $z/H = 0.34$. Profiles over the radial section outside the impeller disk, i.e. $0.3 \leq 2r/D_t \leq 1$ are shown.

Figure 13 compares the present predictions and the previous E-L / LES results for azimuthally averaged radial profiles of radial, tangential and axial mean solid velocity to the experimental data from Guha et al. (2007). The previous E-L / LES results show mostly better agreement with the experimental data than the present baseline prediction. However, at the height $z/H = 0.34$ where the impeller is located, both approaches fail to provide a reasonable representation of the experimental data. At the other two heights, namely $z/H = 0.075$ and $z/H = 0.782$, the agreement between the baseline prediction and the experimental data is generally acceptable except for the tangential velocity at $z/H = 0.075$, which is obviously overestimated. In a previous E-E / RANS simulation (Guha et al., 2008, Figure 4 (a)) of this case by adopting the $k - \varepsilon$ turbulence model even the direction of the tangential flow in this region was not captured correctly.

Predictions according to all other model variants show only minor differences to the baseline model as shown for drag-SN, disp-FAD, and lift-off in Figure 13. The variants T-0.1, T-0.5, drag-Lane, and vm-off are omitted in Figure 13 as they differ even less from the baseline prediction. This insensitivity of the predictions to various aspects of the interaction between the phases suggests that the observed deviations from the experimental data may originate from the RANS turbulence modeling. Also note that the erratic deviation of the variant disp-FAD from the baseline results found for the test of Nouri and Whitelaw (1992) in the last section does not occur here. This and

the corresponding findings concerning the solid fraction profile mentioned above, are possibly due to impeller rotation speed being much faster here than for the test of Nouri and Whitelaw (1992), which could cause particle suspension to be dominated by the mixing due to the mean flow such that turbulent dispersion no longer plays a significant role.

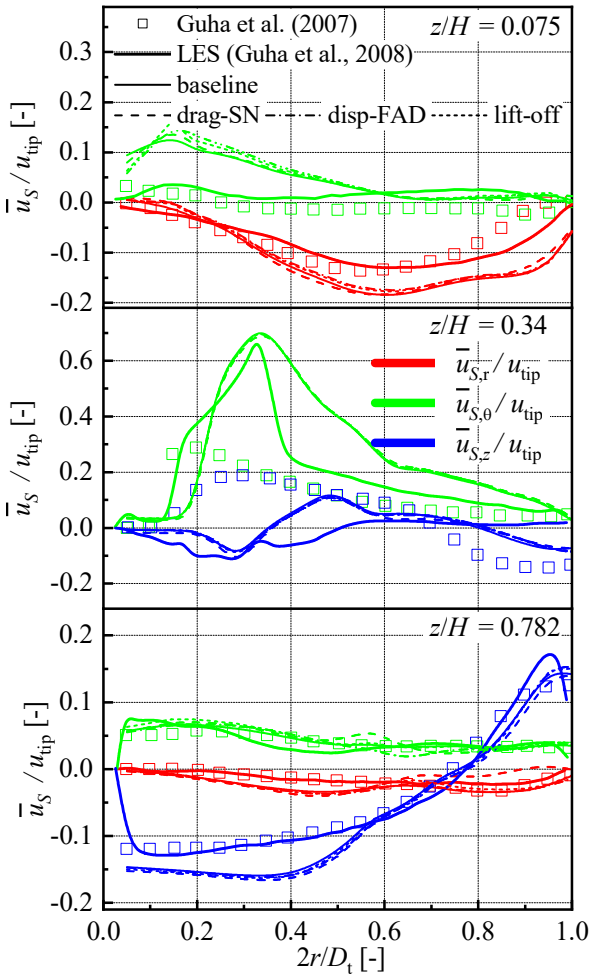

Figure 13. Comparison of the simulation results (lines) according to the baseline model and different model variants listed in Table 8 and the measured data (symbols) from Guha et al. (2007) for azimuthally averaged radial profiles of the radial (red), tangential (green), and axial (blue) components of mean solid velocity. The E-L / LES results (thick solid lines) from Guha et al. (2008) are shown for comparison as well. Radial profiles over the entire tank radius are shown at different heights as indicated on each panel.

5.2.3 Tests from Montante et al. (2012)

Figure 14 compares the baseline predictions for the axial profiles of the radial and axial mean liquid velocity to the experimental data from Montante et al. (2012) at the radial position of $2r/D_t = 0.88$. According to the experimental results, increasing the diameter of the suspended glass particles from 0.115 to 0.775 mm while keeping the average solids loading at $\alpha_{S,ave} = 0.05\%$ apparently does not change the radial velocity component but tends to decrease the axial component in the height range above the impeller, i.e. for $0.3 \leq z/H \leq 0.6$. On the other hand, increasing the average solids loading from 0.05% to 0.15% while keeping the particle diameter of 0.775 mm results in a decrease in the magnitude of the axial component outside the impeller stream, namely

for $0.2 \leq z/H \leq 0.3$ and $0.45 \leq z/H \leq 0.6$. The agreement of the baseline predictions with the experimental data is overall acceptable with notable deviations seen in the impeller stream for the radial velocity and near the tank bottom and the liquid surface in the tangential velocity. Despite these significant absolute deviations, the corresponding predictions are able to represent most of the trends concerning variation of particle size and solid fraction.

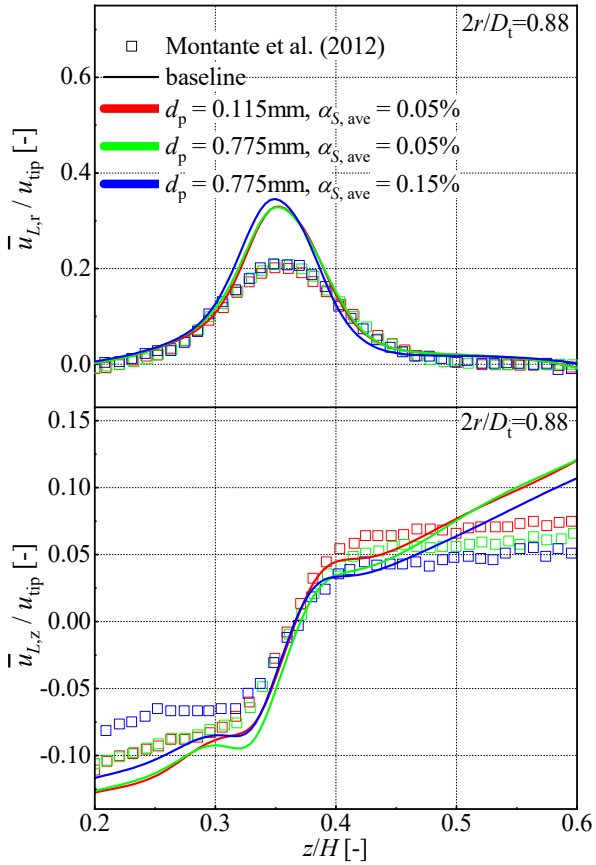

Figure 14. Comparison of the simulation results for the baseline model (lines) and measured data (symbols) from Montante et al. (2012) for the radial and axial components of mean liquid velocity. Axial profiles restricted to the height range of $0.2 \leq z/H \leq 0.6$ are shown at the radial position of $2r/D_t = 0.88$ and for different operation conditions (indicated by different colors) concerning particle size and solids loading.

A similar comparison concerning the fluctuating liquid velocity is shown in Figure 15. For this parameter, experimental results are provided for the radial and axial components at two radial positions $2r/D_t = 0.88$ and $2r/D_t = 0.96$. As seen from the experimental data, overall the magnitude of the radial and axial velocity components increases both with increasing mean solids loading and with increasing particle size. The baseline predictions agree well with the experimental data for the radial velocity fluctuations, while notable deviations are seen for the axial component. The predictions do not change too much between the three different operation conditions so that no clear dependency on particle size or solid fraction can be distinguished.

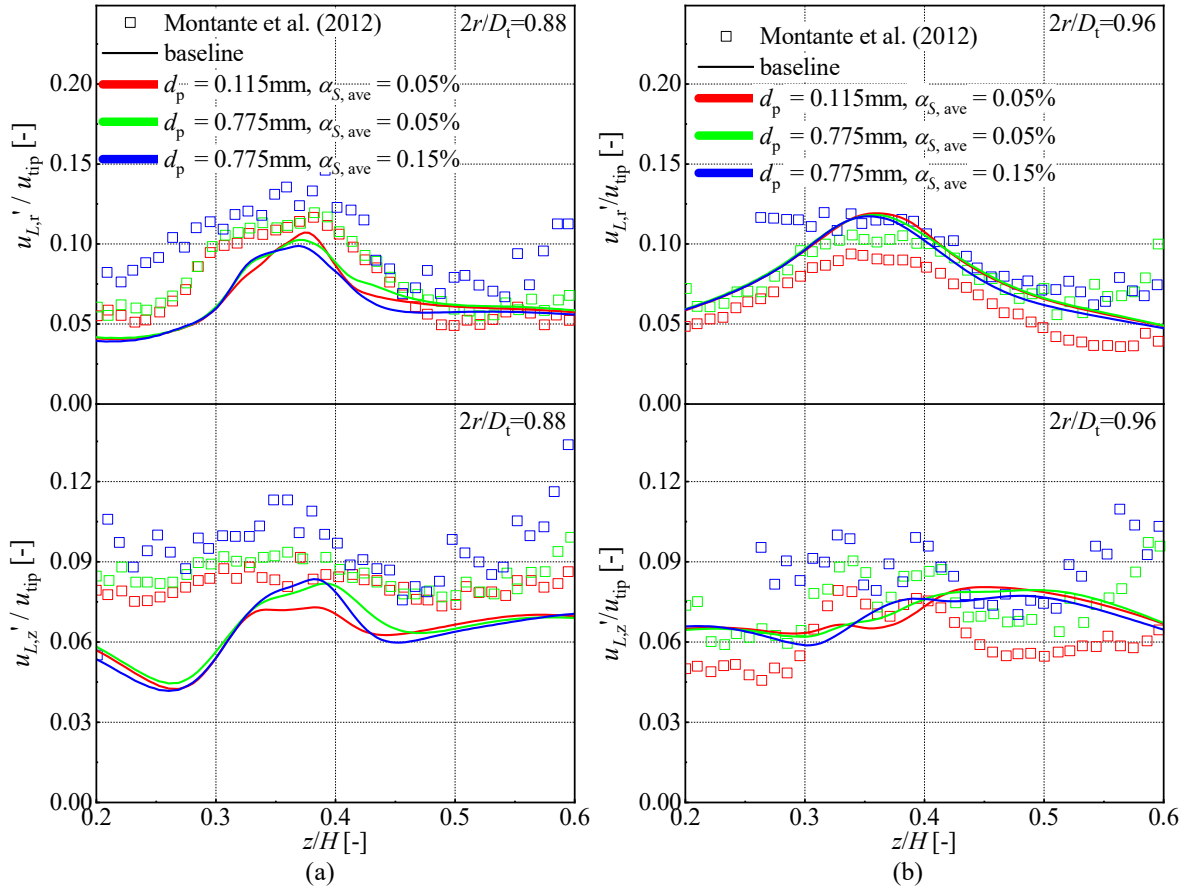

Figure 15: Comparison of the simulation results for the baseline model (lines) and measured data (symbols) from Montante et al. (2012) for the radial and axial components of fluctuating liquid velocity. Axial profiles restricted to the height range of $0.2 \leq z/H \leq 0.6$ are shown for different operation conditions (indicated by different colors) concerning particle size and solids loading at the radial position of (a) $2r/D_t = 0.88$ and (b) $2r/D_t = 0.96$.

5.2.4 Tests from Tamburini et al. (2013)

The tests from Tamburini et al. (2013) provide data for the radially averaged axial profiles of solid fraction at the two impeller rotation speeds of 300 and 600 rpm at the same particle size and average solid fraction. As seen from Figure 16, the measured solid fraction for both values of Ω decreases starting from the tank bottom and reaches a minimum near the location of the impeller, i.e. at $z/H \approx 0.35$. For Ω = 300 rpm the profile then is almost flat between $0.4 \leq z/H \leq 0.8$, while for Ω = 600 rpm it increases steadily. For both values of Ω the solid fraction reaches a maximum around $z/H \approx 0.9$ and then decreases again towards the liquid surface. In the upper/lower part of the tank the solid fraction is higher for the higher/lower value of the rotation rate, with the crossover point located around $z/H \approx 0.6$. This is obviously due to the fact that at a higher impeller rotation speed, a larger amount of particles can be suspended into the upper part of the tank. These qualitative features above are well captured by the predictions except for the flat part of the profile at Ω = 300 rpm. Quantitatively, the agreement is very good at Ω = 600 rpm except close to the tank bottom and liquid surface, where predicted values are too high. At Ω = 300 rpm the prediction suffers under- and overestimations in the impeller stream and in the region near the top wall, respectively. Overall the agreement is still reasonable.

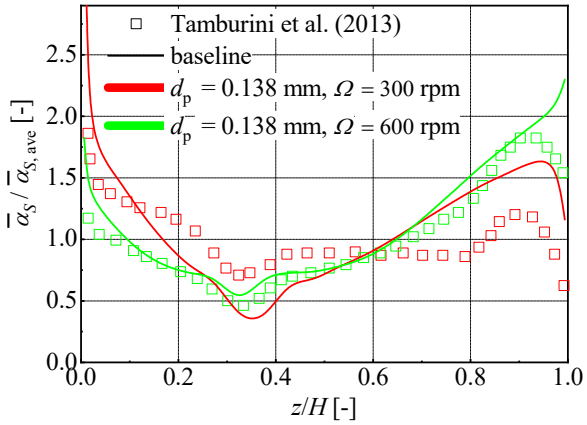

Figure 16. Comparison of the simulation results for the baseline model (lines) and measured data (symbols) from Tamburini et al. (2013) for the solid fraction. Radially averaged axial profiles over the entire tank height are shown.

6 SUMMARY AND CONCLUTIONS

This paper is devoted to the establishment of a two-fluid Euler-Euler model for solid-liquid flows in stirred tanks. Focus has been on the modeling of interfacial forces which include drag, lift, virtual mass, and turbulent dispersion. Based on a comprehensive review of existing results from analytical, numerical, and experimental studies a set of closure relations representing the best currently available description of each aspect has been proposed as a baseline model. Several other model variants that originate from different combinations of interfacial force correlations were considered to highlight the importance of various aspects. To validate the model, a data set comprising mean liquid and solid velocities, turbulent fluctuations and solid fraction measurements was assembled from different sources in the literature. In this way all aspects of the overall model could be assessed.

Single-phase test cases were considered first to provide a reference for the assessment of the two phase flow simulations. The SSG RSM turbulence model in conjunction with the mixing-plane MRF method were adopted. The comparisons together with those from Shi and Rzehak (2018) for both the mean and fluctuating velocities have shown that good predictions are obtained at lower rotation speeds Ω up to ≈ 200 rpm, while deviations occur at higher values certainly from 850 rpm on. In the latter case only qualitative features of the data are reproduced. Although reasonable agreement for engineering purposes in line with previous works (Murthy and Joshi 2008, Shi and Rzehak, 2018) was found, improvements to the SSG RSM clearly remain desirable, which is still the subject of ongoing research (Launder and Sandham, 2002; Morsbach, 2016).

On the basis of these findings, investigation of the two-phase test cases proceeded with the proposed baseline model and seven reduced model variants summarized in Table 8. In particular, the value of the constant as $C_T = 0.224$ determining the integral timescale T_L^L was verified from the axial and radial profiles of the solid fraction. In addition, the necessity to modify the drag correlation of Schiller and Naumann (1933) by a Stokes-number dependent factor, namely Eqs. (18) and (19) in the presently proposed model, could be deduced from these data as well as the need for a Stokes number dependence in the turbulent dispersion, which is contained in the PDF-based model of Reeks (1991) and de Bertodano (1998) but not in the FAD approach of Burns et al., 2004). Lift and virtual mass forces were found negligible in the present test cases. However, these findings are strongly interdependent on one another. For example with a previous drag

963 modification factor from Lane et al. (2005), the lift force did have a significant impact on the results.
964 Therefore, in general it is recommended to use a complete model, accounting for possible effects
965 of lift and virtual mass as well as turbulent dispersion and a modified drag force.

966 The capability of the baseline model in reproducing the fluid flow field as well as in describing the
967 change in solid fraction distribution due to the change in impeller rotation speed was then assessed.
968 Good agreement with the experimental data was obtained for the mean liquid velocity and the solid
969 fraction, while for the liquid velocity fluctuation the agreement was only mediocre. This deviation
970 originates partly from the SSG RSM turbulence model, from which even in the single-phase tests
971 the fluctuation were not captured very well. In addition, neglect of the turbulence modulation due
972 to the presence of the dispersed phase (PIT), for which advanced models are still in preparation
973 (Ma, 2017), may also contribute.

974 Concerning further model development, including a model for the PIT is clearly needed. The use
975 of DNS simulations like in the work of Ma (2017) appears most promising in this direction. There
976 the anisotropic nature of the PIT should be taken into account (Parekh and Rzehak, 2018; Ma et
977 al., 2020). In addition, the model for the modification of the drag force due to turbulence is still in
978 a preliminary stage. The validity of the presently proposed correlation, Eq. (19), in the range of
979 $St > 1$ is still uncertain. Further data, either from experiment of from DNS simulation, are needed
980 on this range. In addition, inclusion of the lengthscale ratio d_p/Λ as a third parameter is necessary
981 for a complete description.

982 The development of better models should be accompanied by the acquisition of more accurate and
983 more comprehensive data for validation. In particular the availability of mean liquid and solid
984 velocities, turbulent fluctuations and solid fractions for the same configuration would be very
985 beneficial to interpret the simulation results. Also parametric variations of particle size, density
986 ratio, mean solids loading, and impeller rotation speed are largely lacking. Finally, the investigation
987 of polydisperse flows would be highly relevant to technical applications.

988 ## 7 ACKNOWLEDGEMENT

989 Mr. Pengyu Shi acknowledges support from the Chinese Scholarship Council (CSC).
990 Computational resources were provided by HZDR. We also thank Dr. Graeme Lane for valuable
991 discussions on drag modification, Professor Jos Derksen for advices on the estimation of ratio of
992 lift to drag forces, and Professors Vivek V. Ranade and Martin Lopez-De-Bertodano for valuable
993 discussions on turbulent dispersion.

994 ## 8 APPENDIX A. GRID INDEPENDENCY STUDY

995 Four different grids are employed to ascertain the grid independence as detailed in Table 9. The
996 cumulative distribution of the reprehensive parameters of mesh quality, i.e. the equiangular
997 skewness, the smoothness (maximum ratio of the volume of a cell to that of each neighboring cell),
998 and the aspect ratio (length ratio of the longest edge to the shortest edge), of the finally used mesh
999 3 are plotted in Figure 17. Distributions found for the other meshes behave similarly. The maximum
1000 values of these three parameters are roughly 0.5, 5, and 1.35, indicating a good mesh quality.

1001

1002

1003

Table 9: Parameters for meshes used in grid independency study.

Mesh	Tank volume			Impeller blade			Overall	CPU time (with 32 processors)
	N_r	N_θ	N_z	N_r	N_θ	N_z	N_{tot}	
1	101	72	106	20	2	16	7.7×10^5	64 h
2	123	90	130	24	3	25	1.44×10^6	120 h
3	101	120	120	30	4	30	1.45×10^6	130 h
4	160	120	150	30	4	30	2.88×10^6	300 h

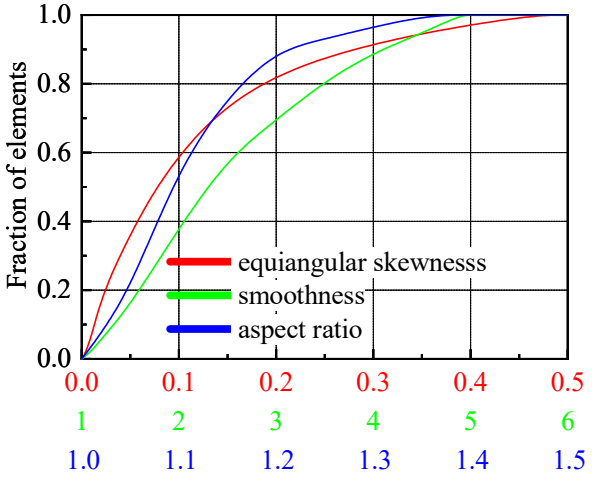

Figure 17. Cumulative distribution of the three measures of mesh quality, namely the equiangular skewness, the smoothness, and the aspect ratio (represented by the red, green, and blue lines, respectively), of mesh 3 as listed in Table 9.

To illustrate the influence of the grid the test case of Guha et al. (2007) is presented, which is most critical due to the high impeller rotation rate (see Table 6 for details of experimental parameters). Results are shown for the axial profiles of mean and fluctuation velocities at $2r/D_t = 0.50$ in the plane mid-way between two baffles. The numerical settings described in section 4.2 are applied.

Figure 18 shows the computational profiles of the three mean velocity components – tangential, radial, and axial – for each mesh. It is seen that the prediction of tangential and axial velocities within the impeller stream is significantly affected by the grid resolution. Results for meshes 3 and 4 show quite good agreement with each other, suggesting that the grid independence has been achieved for mesh 3. A similar comparison concerning the modeled fluctuation velocity $\sqrt{2/3\,k}$ is shown in Figure 19. The difference between the predictions according to meshes 2, 3, and 4 are vanishingly small, indicating a negligible influence of grid resolution here. These observations are consistent with those made in our previous investigation (Shi and Rzehak, 2018). In view of the computational time listed in the last column of Table 9, mesh 3 can be considered to give satisfactory results and meshes with similar average spacings in radial, azimuthal, and axial direction are generated for the other investigated cases (see Table 7).

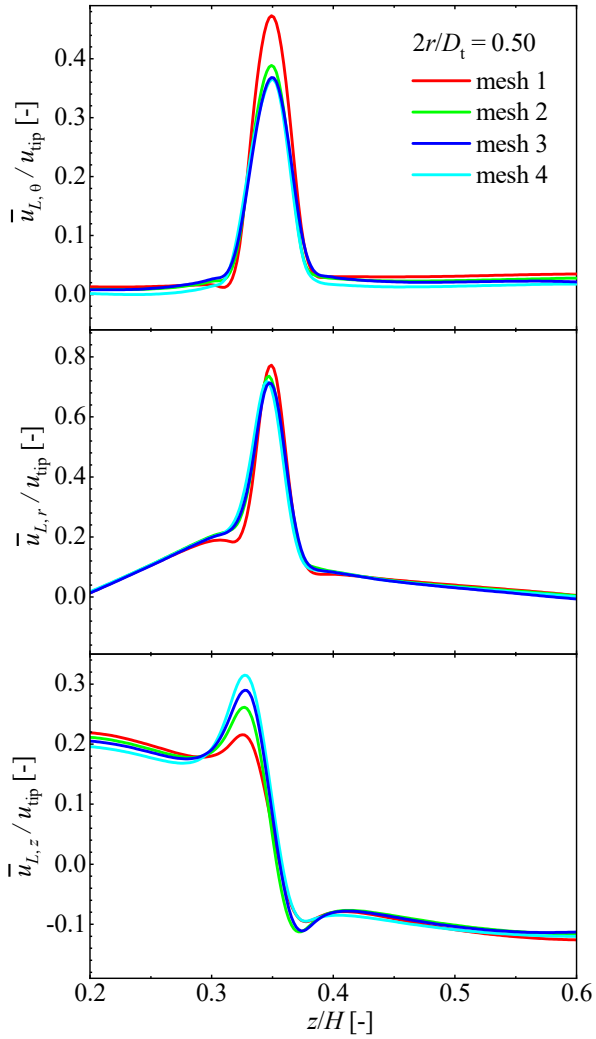

Figure 18. Results of grid independency study for the tangential (top panel), radial (middle panel), and axial (bottom panel) components of mean liquid velocity. The case considered here is the single phase flow in Guha et al. (2007) with an impeller rotation speed of 1000 rpm. Axial profiles restricted to a height range around the impeller are shown at the radial position of $2r/D_t = 0.50$.

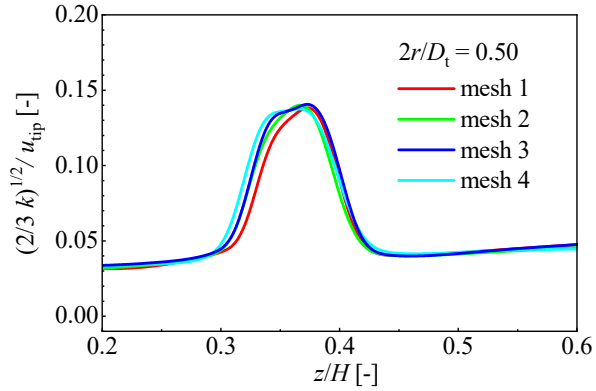

Figure 19. Same as Figure 18 but for the fluctuation velocity.

1033

1034 **9 NOMENCLATURE**

1035

Notation	Unit	Denomination
Latin formula characters		
A_{ij}, **A**	-	anisotropy tensor
C_D	-	drag coefficient
$C_\mathrm{D,0}$	-	stagnant drag coefficient
$C_\mathrm{D,T}$	-	turbulent drag coefficient
C_i	m	clearance between the turbine and tank bottom
C_L	-	lift coefficient
$C_\mathrm{L\omega}$	-	shear-induced lift coefficient
$C_\mathrm{L\Omega}$	-	spin-induced lift coefficient
C_T	-	constant in describing T_L^L
C_VM	-	virtual mass force coefficient
C_Λ	-	constant in describing Λ
d_p	m	particle diameter
D_dis	m	disk diameter
D_i	m	impeller diameter
D_t	m	tank diameter
D_{ij}, **D**	s^{-1}	strain rate tensor
$\boldsymbol{F}$	$\mathrm{N\ m}^{-3}$	force per unit volume
g	$\mathrm{m\ s}^{-2}$	acceleration of gravity
H	m	tank filled height
H_bla	m	blade height
I	-	identity tensor
$J(\epsilon)$	-	function defined by McLaughlin (1991) Eq. (20)
k	$\mathrm{m^2\ s}^{-2}$	turbulent kinetic energy
N	-	number of grid cells
p	Pa	pressure (static)
r	m	radial coordinate
R_{ij}, **R**	$\mathrm{m^2\ s}^{-2}$	Reynolds stress tensor
$Re_\mathrm{p} = u_\mathrm{rel} d_\mathrm{p}/\nu$	-	Reynolds number based on relative velocity
$Re_\omega = \omega d_\mathrm{p}^2/\nu$	-	Reynolds number based on flow vorticity
$Re_\Omega = \Omega d_\mathrm{p}^2/\nu$	-	Reynolds number based on particle rotation rate
$Rr = \Omega d_\mathrm{p}/u_\mathrm{rel}$	-	dimensionless particle rotation rate

$Sr = \omega d_\mathrm{p}/u_\mathrm{rel}$	-	dimensionless flow vorticity or shear rate
St	-	Stokes number
t	s	time
$\mathbf{T}$	N m^{-2}	stress tensor
T_L^L	s	Lagrangian integral timescale following the fluid motion
T_L^S	s	Lagrangian integral timescale following the particle motion
u, $\boldsymbol{u}$	m s^{-1}	resolved velocity
$\boldsymbol{u}'$	m s^{-1}	fluctuating velocity
$\overline{\boldsymbol{u}}$	m s^{-1}	averaged velocity
u_rel	-	slip velocity
$u_\mathrm{term,0}$	m s^{-1}	stagnant terminal velocity
$u_\mathrm{term,T}$	m s^{-1}	turbulent terminal velocity
u_tip	m s^{-1}	impeller tip velocity
W_baf	m	baffle width
W_bla	m	blade width
W_{ij}, $\mathbf{W}$	s^{-1}	rotation rate tensor
y	m	wall normal coordinate
z	m	axial coordinate with the origin at the tank bottom
z_bla	m	axial coordinate with the origin at the impeller disk
Greek Formula characters		
$\bar{\alpha}$	-	phase fraction
β	-	turbulence structure parameter
δ_{ij}	-	Kronecker delta
$\epsilon = \sqrt{Sr/Re_\mathrm{p}}$	-	dimensionless length ratio
ε	m^2 s^{-3}	turbulent dissipation rate
Λ	m	Eulerian longitudinal integral lengthscale
μ	kg m^{-1} s^{-1}	dynamic viscosity
ν	m^2 s^{-1}	kinematic viscosity
θ	rad	azimuthal angle
ρ	kg m^{-3}	density
τ_cross	s	time for a particle to cross an typical eddy
τ_S	s	particle relaxation time
ω	s^{-1}	flow vorticity
Ω	rpm.	impeller rotation speed
$\boldsymbol{\Omega}_{fr}$, Ω_{fr}	s^{-1}	particle angular velocity / rotation rate in the torque-free condition
Latin indices		

body	-	on body
k	-	k^{th} phase
i, j	-	cartesian vector / tensor components
inter	-	on interface
L	-	liquid phase
mol	-	molecular
S	-	solid phase
turb	-	turbulent

10 REFERENCES

Amsden, A.A., 1989. A computer program for chemically reactive flows with sprays. Report of Los Alamos National Laboratory.

Angst, R. and Kraume, M., 2006. Experimental investigations of stirred solid/liquid systems in three different scales: Particle distribution and power consumption. *Chemical Engineering Science* 61, 2864–2870.

ANSYS Inc. ANSYS CFX-Solver Theory Guide: Release 19.2, 2018. Canonsburg, Pennsylvania.

Balachandar, S. and Eaton, J.K., 2010. Turbulent dispersed multiphase flow. *Annual Review of Fluid Mechanics* 42, 111–133.

Barth, T. and Jespersen, D., 1989, January. The design and application of upwind schemes on unstructured meshes. *27th Aerospace sciences meeting*, p366.

Brucato, A., Ciofalo, M., Grisafi, F. and Micale, G., 1998a. Numerical prediction of flow fields in baffled stirred vessels: a comparison of alternative modeling approaches. *Chemical Engineering Science* 53, 3653–3684.

Brucato, A., Grisafi, F. and Montante, G., 1998b. Particle drag coefficients in turbulent fluids. *Chemical Engineering Science* 53, 3295–3314.

Burns, A. D., Frank, T., Hamill, I., Shi, J.-M., 2004. The Favre averaged drag model for turbulence dispersion in Eulerian multi-phase flows, *Proceedings of the 5th International Conference on Multiphase Flow*, ICMF2004, Yokohama, Japan.

Calabrese, R.V. and Middleman, S., 1979. The dispersion of discrete particles in a turbulent fluid field. *AIChE Journal* 25, 1025–1035.

Carletti, C., Montante, G., Westerlund, T. and Paglianti, A., 2014. Analysis of solid concentration distribution in dense solid–liquid stirred tanks by electrical resistance tomography. *Chemical Engineering Science* 119, 53–64.

Chen, Y., Jiang, H. and Huang, X., 2011. Turbulence Properties of Solid-liquid Flow in the Near Wall Region of Stirred Tank. *Journal of Chemical Engineering of Japan* 44, 224–232.

Chen, C.P. and Wood, P.E., 1984. Turbulence closure modeling of two-phase flows. *Chemical Engineering Communications*, 29, 291–310.

1065 Ciofalo, M., Brucato, A., Grisafi, F. and Torraca, N., 1996. Turbulent flow in closed and free-
1066 surface unbaffled tanks stirred by radial impellers. *Chemical Engineering Science* 51, 3557–3573.

1067 Clift, R., Grace, J.R. and Weber, M.E., 2005. Bubbles, drops, and particles. *Courier Corporation*.

1068 Cokljat, D., Slack, M., Vasquez, S.A., Bakker, A. and Montante, G., 2006. Reynolds-stress model
1069 for Eulerian multiphase. *Progress in Computational Fluid Dynamics* 6, 1/3.

1070 Crowe, C.T., Troutt, T.R. and Chung, J.N., 1996. Numerical models for two-phase turbulent flows.
1071 *Annual Review of Fluid Mechanics* 28, 11–43.

1072 Csanady, G.T., 1963. Turbulent diffusion of heavy particles in the atmosphere. *Journal of the*
1073 *Atmospheric Sciences* 20, 201–208.

1074 de Bertodano, M.A.L., 1998. Two fluid model for two-phase turbulent jets. *Nuclear Engineering*
1075 *and Design* 179, 65–74.

1076 Derksen, J.J., 2003. Numerical simulation of solids suspension in a stirred tank. *AIChE Journal* 49,
1077 2700–2714.

1078 Derksen, J.J., 2012. Highly resolved simulations of solids suspension in a small mixing tank.
1079 *AIChE Journal* 58, 3266–3278.

1080 Derksen, J.J., 2018. Eulerian-Lagrangian simulations of settling and agitated dense solid-liquid
1081 suspensions–achieving grid convergence. *AIChE Journal* 64, 1147–1158.

1082 Derksen, J.J. and Van den Akker, H., 1998. Parallel simulation of turbulent fluid flow in a mixing
1083 tank. *International Conference on High-Performance Computing and Networking*, 96–104.

1084 Doroodchi, E., Evans, G.M., Schwarz, M.P., Lane, G.L., Shah, N. and Nguyen, A., 2008. Influence
1085 of turbulence intensity on particle drag coefficients. *Chemical Engineering Journal* 135, 129–134.

1086 Drew, D.A., 2001. A turbulent dispersion model for particles or bubbles. *Journal of Engineering*
1087 *Mathematics* 41, 259–274.

1088 Drew, D.A. and Passman, S.L., 2006. Theory of multicomponent fluids. S*pringer Science &*
1089 *Business Media*.

1090 Fajner, D., Pinelli, D., Ghadge, R.S., Montante, G., Paglianti, A. and Magelli, F., 2008. Solids
1091 distribution and rising velocity of buoyant solid particles in a vessel stirred with multiple impellers.
1092 *Chemical Engineering Science* 63, 5876–5882.

1093 Feng, X., Li, X., Cheng, J., Yang, C. and Mao, Z.S., 2012. Numerical simulation of solid–liquid
1094 turbulent flow in a stirred tank with a two-phase explicit algebraic stress model. *Chemical*
1095 *Engineering Science* 82, 272–284.

1096 Fletcher, D.F. and Brown, G.J., 2009. Numerical simulation of solid suspension via mechanical
1097 agitation: effect of the modeling approach, turbulence model and hindered settling drag law.
1098 *International Journal of Computational Fluid Dynamics* 23, 173–187.

1099 Gabriele, A., Tsoligkas, A.N., Kings, I.N. and Simmons, M.J.H., 2011. Use of PIV to measure
1100 turbulence modulation in a high throughput stirred vessel with the addition of high Stokes number
1101 particles for both up-and down-pumping configurations. *Chemical Engineering Science* 66, 5862–
1102 5874.

Gidaspow, D., 1994. Multiphase flow and fluidization: continuum and kinetic theory descriptions. *Academic Press*.

Gillissen, J.J.J. and Van den Akker, H.E.A., 2012. Direct numerical simulation of the turbulent flow in a baffled tank driven by a Rushton turbine. *AIChE Journal* 58, 3878–3890.

Godfrey, J.C. and Zhu, Z.M., 1994. Measurement of particle-liquid profiles in agitated tanks. *AIChE Symposium Series* 90, 181–185.

Good, G., Ireland, P., Bewley, G., Bodenschatz, E., Collins, L., and Warhaft, Z., 2014. Settling regimes of inertial particles in isotropic turbulence. *Journal of Fluid Mechanics* 759, R3.

Gosman, A.D. and Ioannides, E., 1983. Aspects of computer simulation of liquid-fueled combustors. *Journal of Energy* 7, 482–490.

Gouesbet, G. and Berlemont, A., 1999. Eulerian and Lagrangian approaches for predicting the behaviour of discrete particles in turbulent flows. *Progress in Energy and Combustion Science* 25, 133–159.

Gu, D., Liu, Z., Xu, C., Li, J., Tao, C. and Wang, Y., 2017. Solid-liquid mixing performance in a stirred tank with a double punched rigid-flexible impeller coupled with a chaotic motor. *Chemical Engineering and Processing: Process Intensification* 118, 37–46.

Guha, D., Ramachandran, P.A. and Dudukovic, M.P., 2007. Flow field of suspended solids in a stirred tank reactor by Lagrangian tracking. *Chemical Engineering Science* 62, 6143–6154.

Guha, D., Ramachandran, P.A., Dudukovic, M.P. and Derksen, J.J., 2008. Evaluation of large Eddy simulation and Euler-Euler CFD models for solids flow dynamics in a stirred tank reactor. *AIChE Journal* 54, 766–778.

Guida, A., Nienow, A.W. and Barigou, M., 2010. PEPT measurements of solid–liquid flow field and spatial phase distribution in concentrated monodisperse stirred suspensions. *Chemical Engineering Science* 65, 1905–1914.

Guiraud, P., Costes, J. and Bertrand, J., 1997. Local measurements of fluid and particle velocities in a stirred suspension. *Chemical Engineering Journal* 68, 75–86.

Harrison, S.T., Stevenson, R. and Cilliers, J.J., 2012. Assessing solids concentration homogeneity in Rushton-agitated slurry reactors using electrical resistance tomography (ERT). *Chemical Engineering Science* 71, 392–399.

Ishihara, T., Gotoh, T. and Kaneda, Y., 2009. Study of high–Reynolds number isotropic turbulence by direct numerical simulation. *Annual Review of Fluid Mechanics* 41, 165–180.

Joshi, J. and Nandakumar, K., 2015. Computational modeling of multiphase reactors. *Annual Review of Chemical and Biomolecular Engineering* 6, 347–378.

Kasat, G.R., Khopkar, A.R., Ranade, V.V. and Pandit, A.B., 2008. CFD simulation of liquid-phase mixing in solid–liquid stirred reactor. *Chemical Engineering Science* 63, 3877–3885.

Kataoka, I. and Serizawa, A., 1989. Basic equations of turbulence in gas-liquid two-phase flow. *International Journal of Multiphase Flow* 15, 843–855.

Khopkar, A.R., Kasat, G.R., Pandit, A.B. and Ranade, V.V., 2006. Computational fluid dynamics simulation of the solid suspension in a stirred slurry reactor. *Industrial & Engineering Chemistry Research* 45, 4416–4428.

Kim, S.D. and Kang, Y., 1997. Heat and mass transfer in three-phase fluidized-bed reactors—an overview. *Chemical Engineering Science* 52, 3639–3660.

Kohnen, C., 2000. Experimentelle und numerische Untersuchung der Fluidströmung gerührter Suspensionen. PhD thesis, *TU Braunschweig*, Göttingen.

Lane, G.L., Schwarz, M.P. and Evans, G.M., 2005. Numerical modeling of gas–liquid flow in stirred tanks. *Chemical Engineering Science* 60, 2203–2214.

Launder, B. E., and Sandham, N. D. (Eds.), 2002. Closure strategies for turbulent and transitional flows. *Cambridge University Press*.

Leal, L.G., 1980. Particle motions in a viscous fluid. *Annual Review of Fluid Mechanics* 12, 435–476.

Legendre, D. and Magnaudet, J., 1998. The lift force on a spherical bubble in a viscous linear shear flow. *Journal of Fluid Mechanics* 368, 81–126.

Li, G., Li, Z., Gao, Z., Wang, J., Bao, Y. and Derksen, J.J., 2018. Particle image velocimetry experiments and direct numerical simulations of solids suspension in transitional stirred tank flow. *Chemical Engineering Science* 191, 288–299.

Liu, L. and Barigou, M., 2014. Experimentally Validated Computational Fluid Dynamics Simulations of Multicomponent Hydrodynamics and Phase Distribution in Agitated High Solid Fraction Binary Suspensions. *Industrial & Engineering Chemistry Research* 53, 895–908.

Ljungqvist, M. and Rasmuson, A., 2001. Numerical simulation of the two-phase flow in an axially stirred vessel. *Chemical Engineering Research and Design* 79, 533–546.

Ljungqvist, M. and Rasmuson, A., 2004. The two-phase flow in an axially stirred vessel investigated using phase-Doppler anemometry. *The Canadian Journal of Chemical Engineering* 82, 275–288.

Loth, E., 2001. An Eulerian turbulent diffusion model for particles and bubbles. *International Journal of Multiphase Flow* 27, 1051–1063.

Loth, E., 2008. Quasi-steady shape and drag of deformable bubbles and drops. *International Journal of Multiphase Flow* 34, 523–546.

Lu, Q.Q., 1995. An approach to modeling particle motion in turbulent flows—I. Homogeneous, isotropic turbulence. *Atmospheric Environment* 29, 423–436.

Ma, T., 2017. A Contribution to Turbulence Modelling in Bubbly Flows. *TUD press*.

Ma, T., Lucas, D., Jakirlić, S., and Fröhlich, J., 2020. Progress in the second-moment closure for bubbly flow based on direct numerical simulation data. *Journal of Fluid Mechanics* 883, A9.

Magelli, F., Fajner, D., Nocentini, M. and Pasquali, G., 1990. Solid distribution in vessels stirred with multiple impellers. *Chemical Engineering Science* 45, 615–625.

Maluta, F., Paglianti, A. and Montante, G., 2019. RANS-based predictions of dense solid–liquid suspensions in turbulent stirred tanks. *Chemical Engineering Research and Design* 147, 470–482.

1179 Mazzitelli, I.M., Lohse, D. and Toschi, F., 2003. On the relevance of the lift force in bubbly
1180 turbulence. *Journal of Fluid Mechanics* 488, 283–313.

1181 McLaughlin, J.B., 1991. Inertial migration of a small sphere in linear shear flows. *Journal of Fluid*
1182 *Mechanics* 224, 261–274.

1183 Michaelides, E.E. and Roig, A., 2011. A reinterpretation of the Odar and Hamilton data on the
1184 unsteady equation of motion of particles. *AIChE Journal* 57, 2997–3002.

1185 Micheletti, M., Nikiforaki, L., Lee, K.C. and Yianneskis, M., 2003. Particle concentration and
1186 mixing characteristics of moderate-to-dense solid−liquid suspensions. *Industrial & Engineering*
1187 *Chemistry Research* 42, 6236–6249.

1188 Micheletti, M. and Yianneskis, M., 2004. Study of fluid velocity characteristics in stirred solid-
1189 liquid suspensions with a refractive index matching technique. *Journal of Process Mechanical*
1190 *Engineering* 218, 191–204.

1191 Mei, R., 1992. An approximate expression for the shear lift force on a spherical particle at finite
1192 Reynolds number. *International Journal of Multiphase Flow* 18, 145–147.

1193 Montante, G. and Magelli, F., 2005. Modeling of solids distribution in stirred tanks: analysis of
1194 simulation strategies and comparison with experimental data. *International Journal of*
1195 *Computational Fluid Dynamics* 19, 253–262.

1196 Montante, G. and Magelli, F., 2007. Mixed solids distribution in stirred vessels: experiments and
1197 computational fluid dynamics simulations. *Industrial & Engineering Chemistry Research* 46,
1198 2885–2891.

1199 Montante, G., Paglianti, A. and Magelli, F., 2012. Analysis of dilute solid–liquid suspensions in
1200 turbulent stirred tanks. *Chemical Engineering Research and Design* 90, 1448–1456.

1201 Montante, G., Pinelli, D. and Magelli, F., 2002. Diagnosis of solid distribution in vessels stirred
1202 with multiple PBTs and comparison of two modeling approaches. *The Canadian Journal of*
1203 *Chemical Engineering* 80, 1–9.

1204 Morsbach, C, 2016. Reynolds stress modelling for turbomachinery flow applications. PhD thesis,
1205 *Technische Universität Darmstadt*, Darmstadt.

1206 Mostafa, A.A. and Mongia, H.C., 1987. On the modeling of turbulent evaporating sprays: Eulerian
1207 versus Lagrangian approach. *International Journal of Heat and Mass Transfer* 30, 2583–2593.

1208 Murthy, B. N., and Joshi, J. B., 2008. Assessment of standard k–ε, RSM and LES turbulence
1209 models in a baffled stirred vessel agitated by various impeller designs. *Chemical Engineering*
1210 *Science* 63, 5468–5495.

1211 Nielsen, P., 1993. Turbulence effects on the settling of suspended particles. *Journal of Sedimentary*
1212 *Research* 63, 835–838.

1213 Nouri, J.M. and Whitelaw, J.H., 1992. Particle velocity characteristics of dilute to moderately dense
1214 suspension flows in stirred reactors. *International Journal of Multiphase Flow* 18, 21–33.

1215 Ochieng, A. and Lewis, A.E., 2006. Nickel solids concentration distribution in a stirred tank.
1216 *Minerals Engineering* 19, 180–189.

1217 Ochieng, A. and Onyango, M.S., 2008. Drag models, solids concentration and velocity distribution
1218 in a stirred tank. *Powder Technology* 181, 1-8.

1219 Oshinowo, L.M. and Bakker, A., 2002, February. CFD modeling of solids suspensions in stirred
1220 tanks. *In Symposium on Computational Modeling of Metals, Minerals and Materials, TMS Annual*
1221 *Meeting*, 205–215.

1222 Parekh, J. and Rzehak, R., 2018. Euler-Euler multiphase CFD-simulation with full Reynolds stress
1223 model and anisotropic bubble-induced turbulence. *International Journal of Multiphase Flow* 99,
1224 231–245.

1225 Pearson, B.R., Yousef, T.A., Haugen, N.E.L., Brandenburg, A. and Krogstad, P.Å., 2004. Delayed
1226 correlation between turbulent energy injection and dissipation. *Physical Review E* 70, 056301.

1227 Peirano, E. and Leckner, B., 1998. Fundamentals of turbulent gas-solid flows applied to circulating
1228 fluidized bed combustion. *Progress in Energy and Combustion Science* 24, 259–296.

1229 Pianko-Oprych, P., Nienow, A.W. and Barigou, M., 2009. Positron emission particle tracking
1230 (PEPT) compared to particle image velocimetry (PIV) for studying the flow generated by a pitched-
1231 blade turbine in single phase and multi-phase systems. *Chemical Engineering Science* 64, 4955–
1232 4968.

1233 Poorte, R.E.G. and Biesheuvel, A., 2002. Experiments on the motion of gas bubbles in turbulence
1234 generated by an active grid. *Journal of Fluid Mechanics* 461, 127–154.

1235 Pope, S.B., 2000. Turbulent flows, 1st ed. *Cambridge University Press*.

1236 Pourahmadi, F. and Humphrey, J.A.C., 1983. Modeling solid-fluid turbulent flows with application
1237 to predicting erosive wear. *PhysicoChemical Hydrodynamics* 4, 191–219.

1238 Qi, N., Zhang, H., Zhang, K., Xu, G. and Yang, Y., 2013. CFD simulation of particle suspension
1239 in a stirred tank. *Particuology* 11, 317–326.

1240 Reeks, M.W., 1991. On a kinetic equation for the transport of particles in turbulent flows. *Physics*
1241 *of Fluids A* 3, 446–456.

1242 Reeks M.W., Simonin O., and Fede P., 2017. PDF models for particle transport mixing and
1243 collisions in turbulent flows, *Multiphase Flow Handbook*, 2nd ed., *CRC Press for Taylor Francis*
1244 *Group*, 144–202.

1245 Sardeshpande, M.V., Juvekar, V.A. and Ranade, V.V., 2011. Solid suspension in stirred tanks:
1246 UVP measurements and CFD simulations. *The Canadian Journal of Chemical Engineering* 89,
1247 1112–1121.

1248 Sardeshpande, M.V. and Ranade, V.V., 2012. Computational fluid dynamics modeling of solid
1249 suspension in stirred tanks. *Current Science* 102, 1539–1551.

1250 Sato, Y., Sadatomi, M. and Sekoguchi, K., 1981. Momentum and heat transfer in two-phase bubble
1251 flow—I. Theory. *International Journal of Multiphase Flow* 7, 167–177.

1252 Sato, Y. and Yamamoto, K., 1987. Lagrangian measurement of fluid-particle motion in an isotropic
1253 turbulent field. *Journal of Fluid Mechanics* 175, 183–199.

1254 Sawford, B.L. and Yeung, P.K., 2011. Kolmogorov similarity scaling for one-particle Lagrangian
1255 statistics. *Physics of Fluids* 23, 091704.

Sawford, B.L., Yeung, P.K. and Hackl, J.F., 2008. Reynolds number dependence of relative dispersion statistics in isotropic turbulence. *Physics of Fluids* 20, 065111.

Schiller, L. and Naumann, A., 1933. Fundamental calculations in gravitational processing. *Zeitschrift Des Vereines Deutscher Ingenieure* 77, 318–320.

Shah, R.S.S.R.E., Sajjadi, B., Raman, A.A.A. and Ibrahim, S., 2015. Solid-liquid mixing analysis in stirred vessels. *Reviews in Chemical Engineering* 31, 119–147.

Shan, X., Yu, G., Yang, C., Mao, Z.S. and Zhang, W., 2008. Numerical simulation of liquid− solid flow in an unbaffled stirred tank with a pitched-blade turbine downflow. *Industrial & Engineering Chemistry Research* 47, 2926–2940.

Shi, P. and Rzehak, R., 2018. Bubbly flow in stirred tanks: Euler-Euler/RANS modeling. *Chemical Engineering Science* 190, 419–435.

Shi, P. and Rzehak, R., 2019. Lift Forces on Solid Spherical Particles in Unbounded Flows. *Chemical Engineering Science* 208, 115145.

Shi, P. and Rzehak, R., 2020. Lift Forces on Solid Spherical Particles in Wall-bounded Flows. *Chemical Engineering Science* 211, 115264.

Shlien, D.J. and Corrsin, S., 1974. A measurement of Lagrangian velocity autocorrelation in approximately isotropic turbulence. *Journal of Fluid Mechanics* 62, 255–271.

Shuen, J.S., Chen, L.D. and Faeth, G.M., 1983. Evaluation of a stochastic model of particle dispersion in a turbulent round jet. *AIChE Journal*, 29, 167–170.

Simonin, C. and Viollet, P.L., 1990. Predictions of an oxygen droplet pulverization in a compressible subsonic coflowing hydrogen flow. *Numerical Methods for Multiphase Flows* 91, 65–82.

Snyder, W.H. and Lumley, J.L., 1971. Some measurements of particle velocity autocorrelation functions in a turbulent flow. *Journal of Fluid Mechanics* 48, 41–71.

Sommerfeld, M., Van Wachem, B. and Oliemans, R. eds., 2008. Best practice guidelines for computational fluid dynamics of dispersed multi-phase flows. *European Research Community on Flow, Turbulence and Combustion*.

Spelt, P.D.M. and Biesheuvel, A., 1997. On the motion of gas bubbles in homogeneous isotropic turbulence. *Journal of Fluid Mechanics* 336, 221–244.

Speziale, C. G., Sarkar, S. and Gatski, T. B., 1991. Modeling the pressure–strain correlation of turbulence: an invariant dynamical systems approach, *Journal of Fluid Mechanics* 227, 245–272.

Špidla, M., Sinevič, V., Jahoda, M. and Machoň, V., 2005. Solid particle distribution of moderately concentrated suspensions in a pilot plant stirred vessel. *Chemical Engineering Journal* 113, 73–82.

Sreenivasan, K.R., 1998. An update on the energy dissipation rate in isotropic turbulence. *Physics of Fluids* 10, 528–529.

Tamburini, A., Cipollina, A., Micale, G. and Brucato, A., 2013. Particle distribution in dilute solid liquid unbaffled tanks via a novel laser sheet and image analysis based technique. *Chemical Engineering Science* 87, 341–358.

Tamburini, A., Cipollina, A., Micale, G., Brucato, A. and Ciofalo, M., 2014. Influence of drag and turbulence modeling on CFD predictions of solid liquid suspensions in stirred vessels. *Chemical Engineering Research and Design* 92, 1045–1063.

Tennekes, H., Lumley, J.L. and Lumley, J.L., 1972. A first course in turbulence. *MIT press*.

Trad, Z., Vial, C., Fontaine, J.P. and Larroche, C., 2015. Modeling of hydrodynamics and mixing in a submerged membrane bioreactor. *Chemical Engineering Journal* 282, 77–90.

Unadkat, H., Rielly, C.D., Hargrave, G.K. and Nagy, Z.K., 2009. Application of fluorescent PIV and digital image analysis to measure turbulence properties of solid–liquid stirred suspensions. *Chemical Engineering Research and Design* 87, 573–586.

Vassilicos, J.C., 2015. Dissipation in turbulent flows. *Annual Review of Fluid Mechanics* 47, 95–114.

Virdung, T. and Rasmuson, A., 2007. Solid-liquid flow at dilute concentrations in an axially stirred vessel investigated using particle image velocimetry. *Chemical Engineering Communications* 195, 18–34.

Wadnerkar, D., Tade, M.O., Pareek, V.K. and Utikar, R.P., 2016. CFD simulation of solid–liquid stirred tanks for low to dense solid loading systems. *Particuology* 29, 16–33.

Wang, F., Wang, W., Wang, Y. and Mao, Z., 2003. CFD simulation of solid-liquid two-phase flow in baffled stirred vessels with Rushton impellers. *Proceedings of the 3rd International Conference on CFD in the Minerals and Process Industries*, 287–292.

Wang, G., Ge, L., Mitra, S., Evans, G.M., Joshi, J.B. and Chen, S., 2018. A review of CFD modeling studies on the flotation process. *Minerals Engineering* 127, 153–177.

Wang, S., Jiang, X., Wang, R., Wang, X., Yang, S., Zhao, J. and Liu, Y., 2017. Numerical simulation of flow behavior of particles in a liquid-solid stirred vessel with baffles. *Advanced Powder Technology* 28, 1611–1624.

Werner, S., Kaiser, S. C., Kraume, M., and Eibl, D., 2014. Computational fluid dynamics as a modern tool for engineering characterization of bioreactors. *Pharmaceutical Bioprocessing* 2, 85–99.

Wilcox, D. C., 2006. Turbulence Modeling for CFD. *DCW-Industries* 3rd ed.

Wu, H., Patterson, G.K. and Van Doorn, M., 1989. Distribution of turbulence energy dissipation rates in a Rushton turbine stirred mixer. *Experiments in Fluids* 8, 153–160.

Wu, J., Wang, S., Graham, L., Parthasarathy, R. and Nguyen, B., 2011. High solids concentration agitation for minerals process intensification. *AIChE Journal* 57, 2316–2324.

Yamazaki, H., Tojo, K. and Miyanami, K., 1986. Concentration profiles of solids suspended in a stirred tank. *Powder Technology* 48, 205–216.

Yang, C. and Mao, Z.S., 2014. Numerical simulation of multiphase reactors with continuous liquid phase. *Academic Press*.

Yeung, P.K., 2001. Lagrangian characteristics of turbulence and scalar transport in direct numerical simulations. *Journal of Fluid Mechanics* 427, 241–274.

1332 Yeung, P.K., Pope, S.B. and Sawford, B.L., 2006. Reynolds number dependence of Lagrangian
1333 statistics in large numerical simulations of isotropic turbulence. *Journal of Turbulence* 7, N58.

1334 Yudine, M.I., 1959. Physical considerations on heavy-particle diffusion. *Advances in Geophysics*
1335 6, 185–191.

1336 Zhou, Q. and Leschziner, M.A., 1991. A time-correlated stochastic model for particle dispersion
1337 in anisotropic turbulence. *In 8th Symposium on Turbulent Shear Flows* 1, 10-3.